Tropical Multidecadal and Interannual Climate Variability in the NCEP–NCAR Reanalysis

Muthuvel Chelliah and Gerald D. Bell

Climate Prediction Center, NCEP/NWS/NOAA, Washington D.C.

ABSTRACT

The leading tropical multidecadal mode (TMM) and tropical interannual (ENSO) mode in the 52-yr (1949–2000) NCEP–NCAR reanalysis are examined for the December–February (DJF) and June–August (JJA) seasons based on seasonal tropical convective rainfall variability and tropical surface (land + ocean) temperature variability. These combined modes are shown to capture 70%–80% of the unfiltered variance in seasonal 200-hPa velocity potential anomalies in the analysis region of 30°N–30°S. The TMM is the dominant mode overall, accounting for 50%–60% of the total unfiltered variance in both seasons, compared to the 22%–24% for ENSO.

The robustness of the tropical multidecadal mode is addressed, and the results are shown to compare favorably with observed station data and published results of decadal climate variability in the key loading regions. The temporal and spatial characteristics of this mode are found to be distinct from ENSO.

The TMM captures the global climate regimes observed during the 1950s–60s and 1980s–90s, and the 1970s transition between these regimes. It provides a global-scale perspective for many known aspects of this decadal climate variability (i.e., surface temperature, precipitation, and atmospheric circulation) and links them to coherent multidecadal variations in tropical convection and surface temperatures in four core regions: the West African monsoon region, the central tropical Pacific, the Amazon basin, and the tropical Indian Ocean.

During JJA, two distinguishing features of the tropical multidecadal mode are its link to West African monsoon variability and the pronounced zonal wavenumber-1 structure of the 200-hPa streamfunction anomalies in the subtropics of both hemispheres. During DJF a distinguishing feature is its link between anomalous tropical convection and multidecadal variations in the North Atlantic Oscillation (NAO). For the linear combination of the TMM and ENSO the strongest regressed values of the wintertime NAO index are found when their principal component (PC) time series are out of phase.

In the Tropics and subtropics the linearly combined signal for the TMM and ENSO is strongest when their PC time series are in phase and is weakest when they are out of phase. This result suggests a substantial modulation of the ENSO teleconnections by the background flow. It indicates stronger La Niña teleconnections during the 1950s–60s, compared to stronger El Niño teleconnections during the 1980s–90s. Although this study addresses the linear ENSO–TMM interference, the results also suggest that interactions between the two modes may help to explain the stronger El Niño episodes observed during the 1980s–90s compared to the 1950s–60s.

1. Introduction

There is an ongoing effort to better understand the coherent multidecadal fluctuations in the global climate system that result from interactions between the various components of the climate system itself, such as the oceans, land, and atmosphere. It is generally assumed that the slowly varying sea surface temperatures (SSTs) are the dominant source of this variability (e.g., Kawamura et al. 1995a,b; Livezey and Smith 1999; Mo et al. 2001; Hoerling et al. 2001), which has prompted several extended climate simulations using general circulation models (GCMs) forced by the observed near-

global SSTs (Graham 1994; Lau and Nath 1994). Tropical convection is then a primary mechanism by which surface temperature variations are ultimately transmitted to the atmospheric circulation in the Tropics and portions of the extratropics (e.g., Mo and Kousky 1993).

Regional aspects of decadal-scale climate variability are found throughout the global Tropics and extratropics. Morrissey and Graham (1996) have documented a trend toward decreased tropical convective rainfall during 1971–90 over the western portions of both the tropical South and North Pacific, and a trend toward increased rainfall across the central tropical South Pacific (along 10°S). Zhang et al. (1997) and Higgins et al. (2000) documented a similar sense to the convective rainfall fluctuations in this latter region, and noted that the associated atmospheric streamfunction anomalies are global in scale and feature a pronounced zonal wavenumber-1 pattern in the subtropics of both hemispheres.

Corresponding author address: Dr. Muthuvel Chelliah, Rm. 605A, Climate Prediction Center, NCEP/NWS/NOAA/U.S. Dept. of Commerce, 5200 Auth Road, NOAA Science Center, Camp Springs, MD 20746-4304.
E-mail: muthuvel.chelliah@noaa.gov

Over the extratropical North Pacific a strengthening and eastward shift of the wintertime Aleutian low since 1976/77 has been documented and related to a transition from above-average SSTs in the central North Pacific during the 1950s–60s to below-average temperatures during the 1980s–90s (Namias et al. 1988; Trenberth 1990; Trenberth and Hurrell 1994). These SST fluctuations are referred to as the Pacific Decadal Oscillation (PDO) (Trenberth and Hurrell 1994; Latif and Barnett 1994; Mantua et al. 1997), or equivalently the North Pacific Oscillation (Gershunov and Barnett 1998). Using tree ring chronology, Bione et al. (2001) subsequently showed multidecadal variations in the Pacific climate dating back to the 1600s.

For the more recent decades Zhang et al. (1997) noted that the SST difference fields between the 1950s–60s and the 1980s–90s resembled a horseshoe-shaped pattern in the tropical Pacific typical of mature El Niño conditions, and, hence, suggested "ENSO-like" decadal variability. Using annual mean anomalies, Higgins et al. (2000) also noted a similarity between the ENSO-related circulation features and those associated with the leading multidecadal EOF of annual mean rainfall anomalies over the central tropical South Pacific. Garreaud and Battisti (1999) also found evidence for ENSO-like decadal variability in the Southern Hemisphere.

However, Mestas-Nuñez and Enfield (1999) showed for the extended period of 1870–1999 that the leading unrotated multidecadal EOF of global SST anomalies exhibits strong fluctuations with an average periodicity of 40–60 yr. Mestas-Nuñez and Enfield (2001) showed that the dominant SST fluctuations associated with this mode spanned both the Pacific and Atlantic Oceans, and incorporated both the PDO and the Atlantic multidecadal mode. These results are consistent with a growing body of literature suggesting that the temporal and spatial structures of the dominant decadal-scale climate variations differ notably from ENSO (e.g., Kawamura 1994; Kushnir 1994; Gray et al. 1997; Latif et al. 1997; Gershunov and Barnett 1998; Biondi et al. 2001; Chen et al. 2001; Mo et al. 2001; Hoerling et al. 2001).

Focusing on the Atlantic sector, the cool phase of the Atlantic multidecadal mode reflects cooler SSTs at both high latitudes and in the subtropics of the North Atlantic as seen during the 1980s–90s, and the warm phase reflects anomalously warm SSTs in these regions as seen during the 1950s–60s (Delworth et al. 1993, 1997; Kushnir 1994; Hansen and Bezdek 1996; Enfield and Mestas-Nuñez 1999; Enfield et al. 2001). Gray et al. (1997) suggested these SST variations might result from changes in the North Atlantic deep-water formation and the Atlantic thermohaline circulation.

Phase changes in the Atlantic multidecadal mode are accompanied by fluctuations in the West African monsoon system, with an enhanced monsoon seen during the 1950s–60s compared to from the 1970s to the mid-1990s (Folland et al. 1986; Nicholson and Palao 1993;

Rowell et al. 1995; Nicholson 1996; Ward 1998; Thaiw et al. 1998). In turn, variations in the West African monsoon influence the upper-level atmospheric circulation across the tropical Atlantic and Africa in both hemispheres (Hastenrath 1990; G. D. Bell and M. Chelliah 2004, unpublished manuscript), and are likely a contributing factor to the observed decadal variations in North Atlantic hurricane activity (Gray 1990; Landsea and Gray 1992; Goldenberg and Shapiro 1996; Goldenberg et al. 2001).

North Atlantic SST variability has also been associated with multidecadal fluctuations in the wintertime North Atlantic Oscillation (NAO) as defined by Barnston and Livezey (1987). The positive phase of the NAO during the 1980s–90s reflects a stronger Icelandic low with reduced blocking activity over the high latitudes of the North Atlantic compared to the 1950s–60s (Halpert and Bell 1997). Hurrell (1998) showed that these NAO phase changes are associated with dramatic differences in the poleward heat transport, and that they can account for the above-average surface temperatures seen across Eurasia in recent decades.

This SST variability over both the Atlantic and Pacific sectors also appears to be linked to decadal-scale fluctuations in tropical Indian Ocean temperatures. For example, Kawamura (1994) recognized that the cooling of the extratropical North Pacific during the 1980s occurred concurrently with a warming of the tropical Indian Ocean, which Hoerling et al. (2001) indicated was also linked to a warming of the central tropical South Pacific. Hoerling et al. then performed a series of GCM experiments suggesting this combined warming might be a contributing factor to the prolonged positive phase of the NAO and cooler Atlantic Ocean temperatures seen in recent decades.

Chu et al. (1994), Kumar et al. (1999), and Chen et al. (2001) also documented increased convective rainfall over the Amazon basin during the 1980s–90s compared to the 1950s–60s. Chen et al. indicated for the December–February (DJF) season that these decadal variations in Amazon basin rainfall were linked to corresponding changes in the global divergent circulation, particularly over the tropical Pacific and Indian Ocean sectors.

In the current study the coherent decadal fluctuations in tropical convection and surface temperatures over the central Pacific, the West African monsoon region, the Amazon basin, and the Indian Ocean, are shown to constitute the dominant decadal-scale mode of variability in the global Tropics. Because of its link to known multidecadal climate fluctuations in these regions, this mode is subsequently referred to as the "tropical multidecadal mode" (TMM). By comparison, ENSO is the leading interannual mode associated with tropical convective rainfall and SST variability. The analysis also examines the modulation of the ENSO teleconnections by the TMM.

We have chosen to define the tropical multidecadal and ENSO modes in the National Centers for Environ-

mental Prediction (NCEP)–National Center for Atmospheric Research (NCAR) reanalysis (Kalnay et al. 1996) for the 52-yr period 1949–2000 using EOF analyses based on seasonal 200-hPa velocity potential anomalies and surface temperature (land + ocean) anomalies in the region of 30°N–30°S. The use of velocity potential anomalies to define these modes is consistent with their links to anomalous tropical convection and the large-scale divergent circulation (Chen et al. 2001). Seasonal [June–August (JJA) and DJF] rather than annual mean anomalies are used to account for the strong seasonality in tropical convective rainfall variability, and in the associated atmospheric response. Surface temperature (land + ocean) anomalies are used instead of just SST anomalies because of the strong relationship between land surface temperatures and tropical convection (Charney 1975; Xue and Shukla 1993; Zeng et al. 1999; Zeng and Neelin 2000).

The paper is organized with data issues discussed in section 2. The climatological relationship between the seasonal 200-hPa velocity potential, outgoing longwave radiation (OLR), and precipitation, are summarized in section 3. The tropical multidecadal mode and tropical interannual (ENSO) mode are described in section 4. The associated rainfall and surface temperature anomalies are also discussed and compared with station observations in key loading regions. The atmospheric circulation anomalies associated with these individual and combined modes are described in section 5. The main findings are summarized in section 6, and results are discussed in section 7.

2. Data sources

The EOF and regression analyses are based primarily on gridded atmospheric circulation, precipitation rate, and surface temperature data obtained from the NCEP–NCAR reanalysis (Kalnay et al. 1996). The model-derived precipitation rates are based on 6-hourly forecasts. The surface temperature data are based on observed SSTs over water and model-derived surface temperatures over land. Basist and Chelliah (1997) and Chelliah and Ropelewski (2000) have shown that interannual variations in the NCEP–NCAR surface temperatures and mean tropospheric temperatures compare well with independent estimates obtained from the Microwave Sounding Unit (MSU) and from station data archive described by Jones et al. (1991).

While the reanalysis eliminates climate discontinuities related to changes in the model and data assimilation systems, it does not completely resolve problems related to the uneven spatial and temporal distribution of the raw observational data over the 52-yr analysis period (Ebisuzaki et al. 1997; Kistler et al. 2001). Therefore, our results focus on the regions where the loadings can be substantiated with independent data sources and results of previous studies.

The independent data sources include rain gauge–

satellite-based rainfall estimates for the period 1979–95 (Xie and Arkin 1997), the monthly gridded precipitation dataset for the period 1950–98 produced by Hulme (1995), station rain gauge data from the global Historical Climatology Network (GHCN) archived at the National Climatic Data Center (NCDC), gridded monthly mean OLR data for the period 1979–2000, station radiosonde data, and gridded SST data obtained from Smith et al. (1996) for the period 1949–2000.

3. Relationship between 200-hPa velocity potential, OLR, and precipitation

By definition horizontal divergence on a constant pressure surface is equal to the horizontal Laplacian of the velocity potential (Krishnamurti 1971). The divergent wind vectors are oriented perpendicular to the velocity potential contours and directed from low to high values, with speed proportional to the velocity potential gradient. Examination of the 200-hPa climatological mean (1979–2000) conditions during both JJA and DJF indicates that the areas of divergence in the reanalysis (Fig. 1), which coincide with a positive Laplacian of velocity potential (contours), are consistent with the convectively active regions indicated by low OLR values (shading). Consistency between the areas of upper-level convergence and high OLR values is also seen.

Further consistency of the seasonal velocity potential in the reanalysis is established by comparing its temporal variability (Fig. 2a) with that of the seasonal OLR measurements (Fig. 2b, see also Chelliah and Arkin 1992) and Climate Prediction Center (CPC) merged analysis of precipitation estimates (CMAP; Fig. 2c; Xie and Arkin 1997). This consistency between the three datasets is also described by Janowiak et al. (1998), and supports the use of seasonal 200-hPa velocity potential anomalies to define the leading tropical modes over the longer period of 1949–2000.

4. Leading tropical multidecadal and interannual modes during JJA and DJF

a. Principal component time series

The tropical multidecadal (interannual) mode represents the leading covariance-based unrotated EOF of 5-yr running mean low-pass (high-pass)-filtered seasonal 200-hPa velocity potential anomalies in the region of 30°N–30°S based on the 52-yr (1949–2000) NCEP–NCAR reanalysis. The covariance matrix is used in order to capture the variance maxima of the actual seasonal anomalies, rather than those of the standardized anomalies.

During both JJA and DJF the principal component (PC) time series of the tropical multidecadal mode (thick solid curve, Figs. 3a and 4a) indicates quasi-constant negative values during the 1950s–60s and positive values during the 1980s–90s, with a major transition oc-
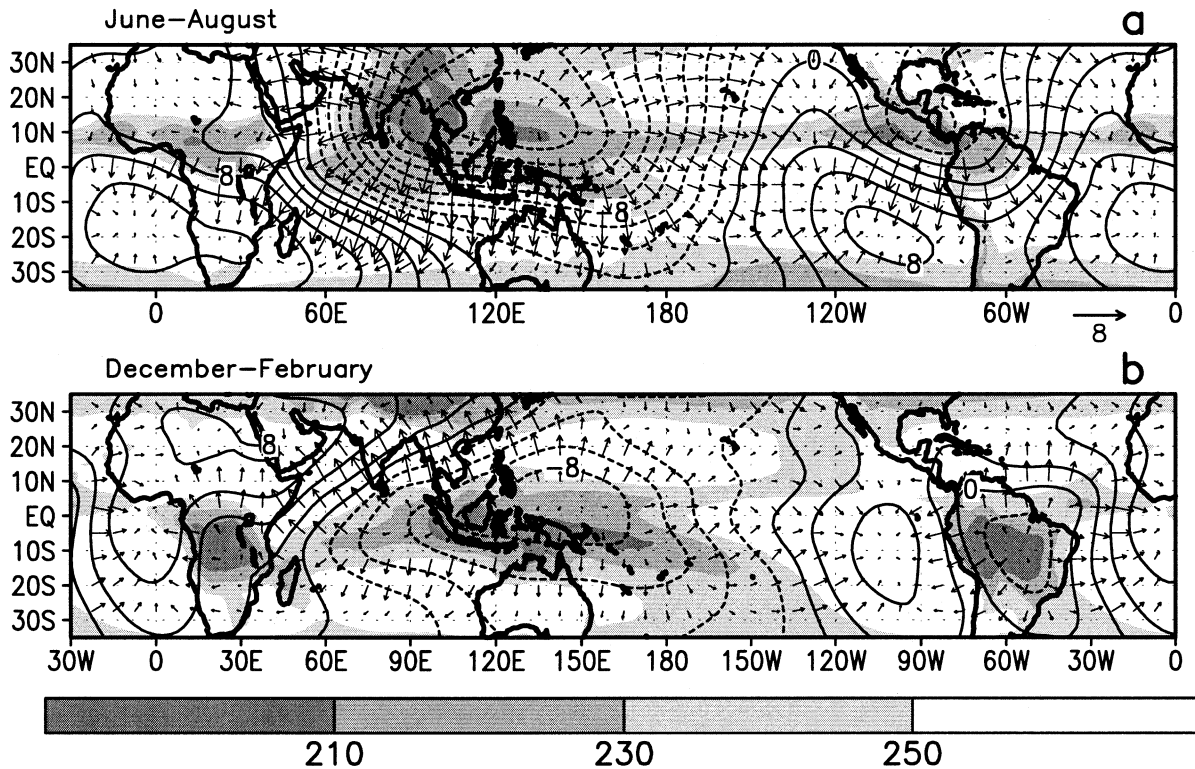
Climatological Mean

FIG. 1. 1979–2000 climatological mean OLR (shaded, W m^{-2}), 200-hPa velocity potential (contours, interval is 2×10^6 m^2 s^{-1}), and divergent wind vectors (m s^{-1}) for (a) JJA and (b) DJF. The divergent vector wind scale is located below (a).

curring during the 1970s. This transition between climate states is also seen in the PC time series of the leading multidecadal EOF of seasonal tropical surface (land + sea) temperature anomalies (dashed curve, Fig. 3a), which is correlated at 0.87 with that of the velocity potential anomalies.

Although these time series can be approximated by an overall upward trend, this characterization can be misleading because the upward trend is seen mainly only during the 1970s. Mestas-Nuñez and Enfield (1999) also showed a similar transition in the PC time series associated with the leading multidecadal EOF of annual mean SST anomalies, and found that it was consistent with the dominant 40–60-yr period of multidecadal fluctuations seen in the longer record dating back to 1870. We, therefore, refer to these coherent low-frequency fluctuations as the "tropical multidecadal mode" rather than associating them with a single linear trend.

The PC time series of the leading tropical interannual mode captures ENSO (thin curve, Figs. 3a, 4a), with the positive (negative) phase corresponding to El Niño (La Niña). The time series exhibit comparatively small-amplitude fluctuations prior to 1972, consistent with van Loon and Shea (1985) and Ropelewski et al. (1992), and larger-amplitude fluctuations beginning with the strong 1982/83 El Niño. These decadal variations in

ENSO strength are significant at the 95% confidence level, according to a Monte Carlo simulation of 1000 scenarios that allows for a 1-yr lag between successive seasons. This result is consistent with the finding of Nicholls et al. (1996), Latif et al. (1997), Harrison and Larkin (1996), and Mestas-Nuñez and Enfield (2001).

For the entire 30°N–30°S analysis region most of the unfiltered variance in seasonal 200-hPa velocity potential anomalies (82% in JJA and 70% in DJF) is captured by the two leading tropical modes. The tropical multidecadal mode accounts for 59% (48%) of the unfiltered seasonal variance during JJA (DJF), while the ENSO mode accounts for 22%–24% in both seasons. Regionally, the amount of unfiltered variance captured by the two modes is substantial, generally averaging 60%–80%+ (shading, Figs. 3b, 4b) in areas with large standard deviation in both velocity potential (contours) and tropical convective rainfall (recall Figs. 2c,d).

The spatial structure and total explained variance (Figs. 3c,d and 4c,d) of the two modes remain unaffected when the EOF calculations are performed on the unfiltered seasonal data, and when the unfiltered EOFs are subjected to Varimax rotation. They also remain unaffected when the modes are separated using a 7-yr running mean low-pass (LP) filter, when the EOF analysis is performed on smaller analysis domains (25°N–
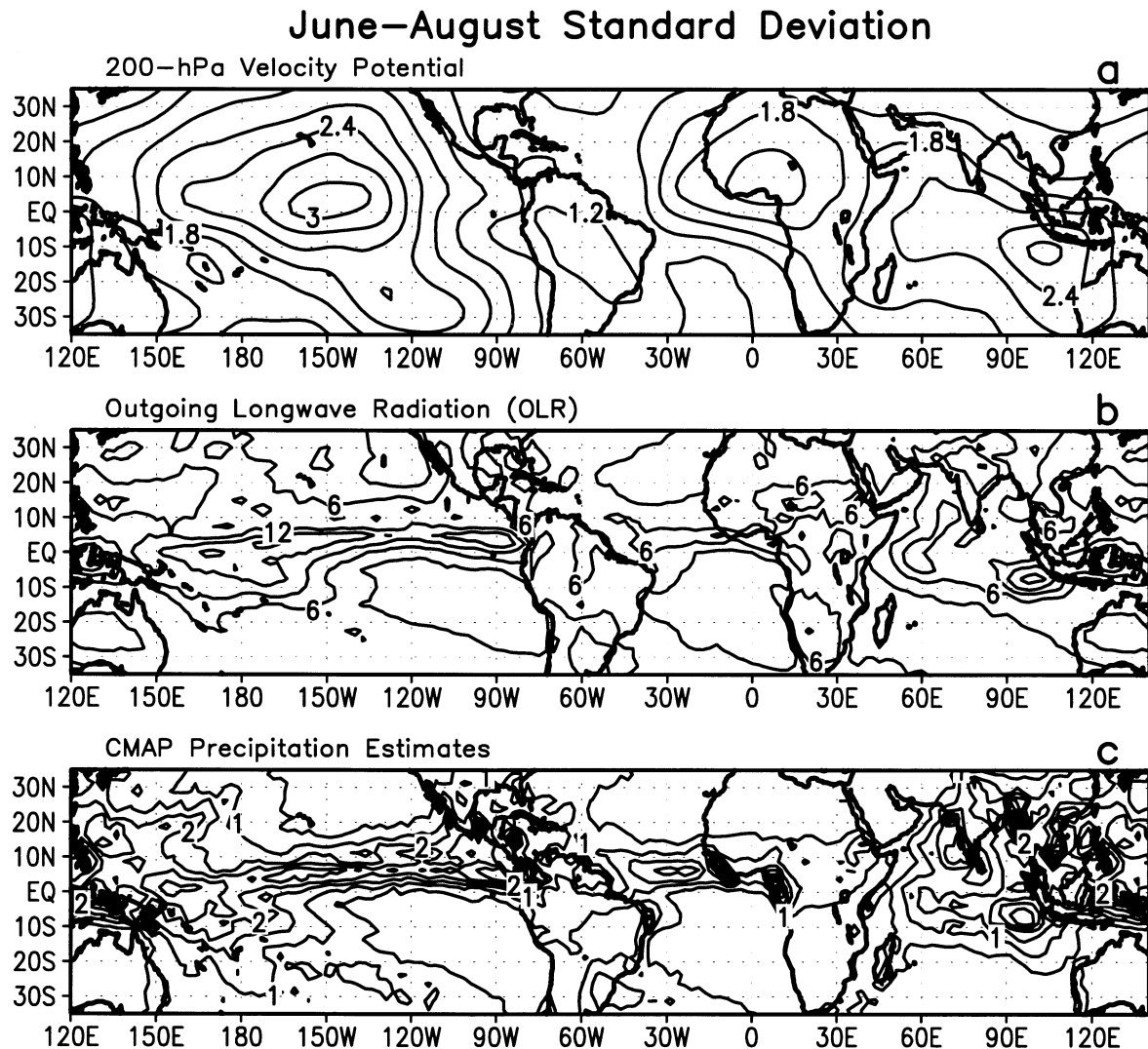
June–August Standard Deviation

200-hPa Velocity Potential

Outgoing Longwave Radiation (OLR)

CMAP Precipitation Estimates

FIG. 2. Std dev of JJA seasonal mean (a) 200-hPa velocity potential (interval is 0.3×10^6 m^2 s^{-1}), (b) OLR (interval is 3 W m^{-2}), and (c) CMAP seasonal precipitation estimates of Xie and Arkin (1997; interval is 0.5 mm day^{-1}). Anomalies are departures from the 1979–2000 base period seasonal means.

25°S and 20°N–20°S), and when the analysis period is reduced to 1961–90. In each case, the modes are well separated from each other (North et al. 1982) and from the higher modes.

b. Tropical multidecadal mode: 200-hPa velocity potential, divergence, and precipitation rate

In both seasons the tropical multidecadal mode features a three-celled pattern of 200-hPa velocity potential and divergence anomalies (Figs. 3c, 4c), and accounts for more than 60% of the unfiltered variance in seasonal velocity potential anomalies (shading) in each of the high-variance regions (contours, Figs. 3b, 4b). It also accounts for 20%–50% of the unfiltered seasonal precipitation rate variance (shading, Figs. 5a,b) and 55%–

80% of the 5-yr running mean LP-filtered variance (Figs. 6a,b) in each region.

During JJA the positive phase of the TMM seen during the 1980s–90s features anomalous upper-level divergence (Fig. 3c) and above-average precipitation rates (Fig. 5a) over the Amazon basin and the eastern tropical North Pacific along the mean position of the ITCZ, with flanking cells of anomalous upper-level convergence and below-average precipitation rates over the West African monsoon region and the central equatorial Pacific. Conversely, its negative phase seen during the 1950s–60s features above-average precipitation rates over the central equatorial Pacific and an enhanced West African monsoon, with compensating subsidence over the Amazon basin. This signal is nearly identical to that associated with the leading multidecadal EOF of seasonal
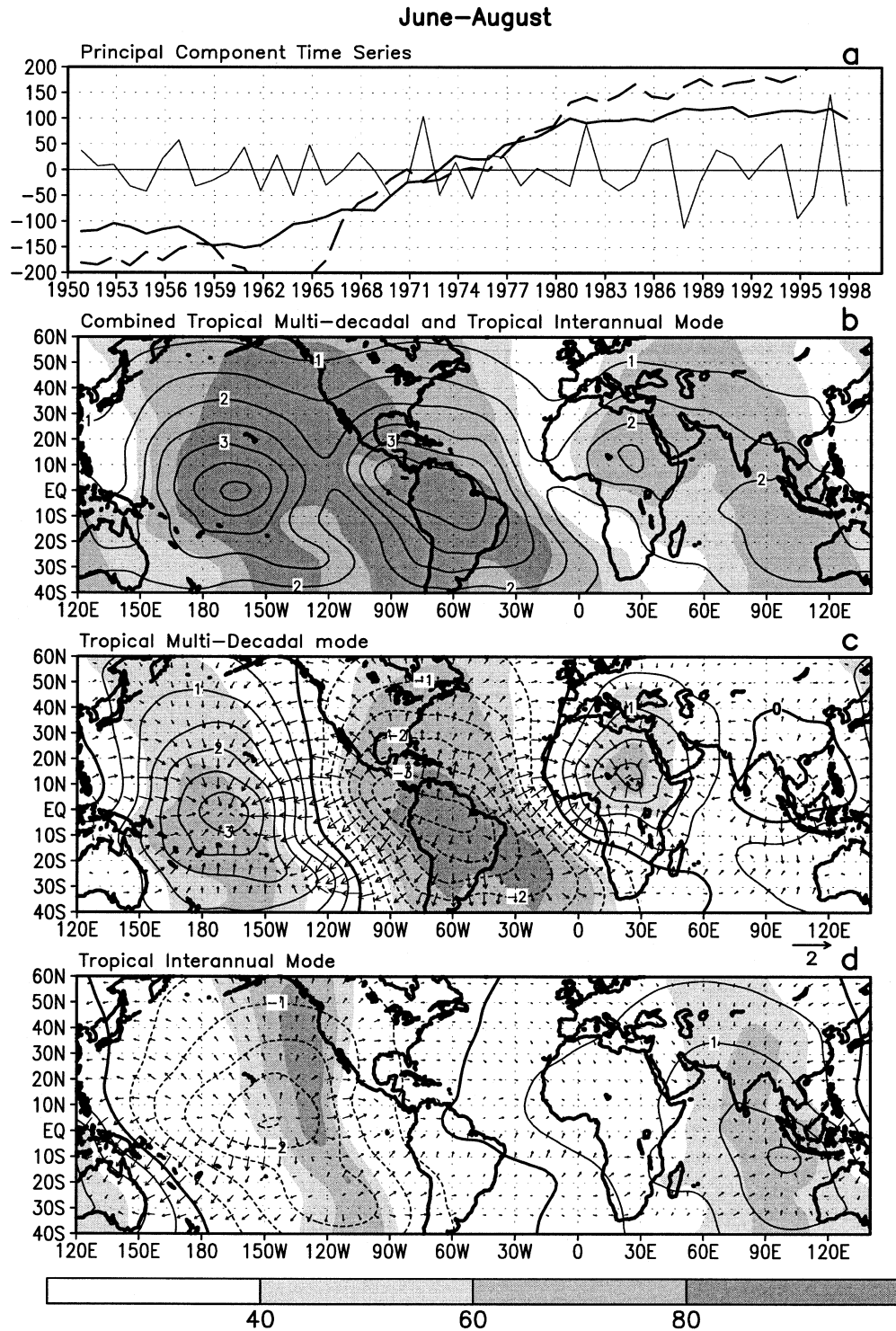
FIG. 3. JJA (a) PC time series for the TMM (thick solid), tropical interannual mode (ENSO, thin solid), and leading multidecadal EOF of seasonal surface temperature anomalies (dashed). Shading shows percent of explained variance of unfiltered seasonal 200-hPa velocity potential anomalies by the (b) combined TMM and ENSO, (c) TMM, and (d) ENSO. (b) The 1949–2000 std dev of seasonal 200-hPa velocity potential anomalies (contours, interval is 5×10^6 m^2 s^{-1}). (c), (d) The seasonal 200-hPa velocity potential loadings [contours, interval is 0.5×10^6 m^2 s^{-1} (std dev)$^{-1}$ of the TMM and ENSO, respectively]. The associated 200-hPa divergent vector wind anomalies [m s^{-1} (std dev)$^{-1}$ of the model] are also plotted, with vector scale located above (d).
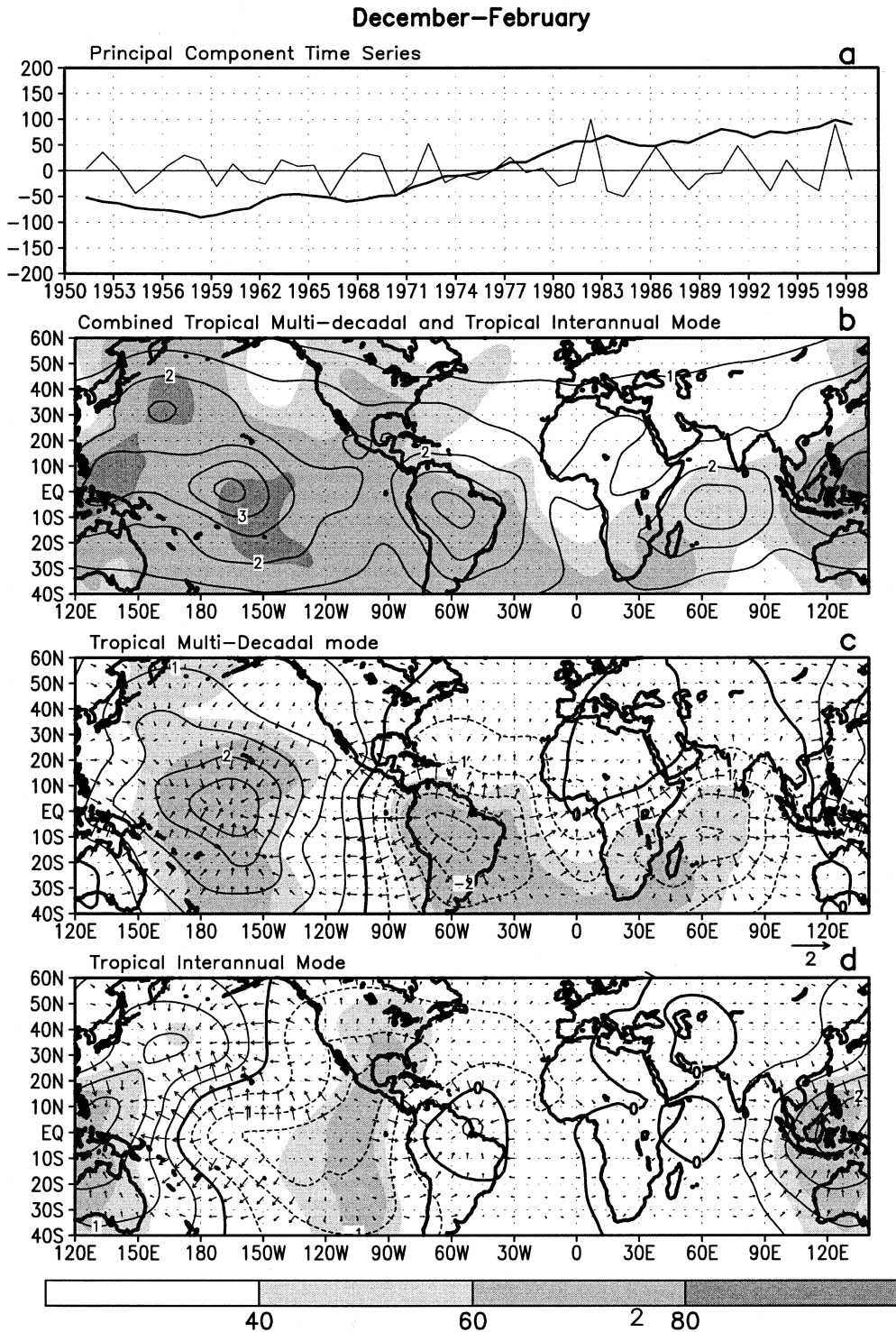
FIG. 4. As in Fig. 3, except for the DJF season.

tropical surface temperature (land + ocean) anomalies (shown for JJA, Figs. 5c, 6c), indicating that both EOF analyses are capturing similar decadal-scale climate anomalies.

During DJF the positive phase of the TMM features above-average precipitation rates again over the Amazon basin and also over the equatorial Indian Ocean (contours, Fig. 5b), with the main area of compensating subsidence shifted to the central equatorial Pacific. In its negative phase the main area of anomalous ascending

Multi–Decadal EOF: Seasonal Precipitation Rates
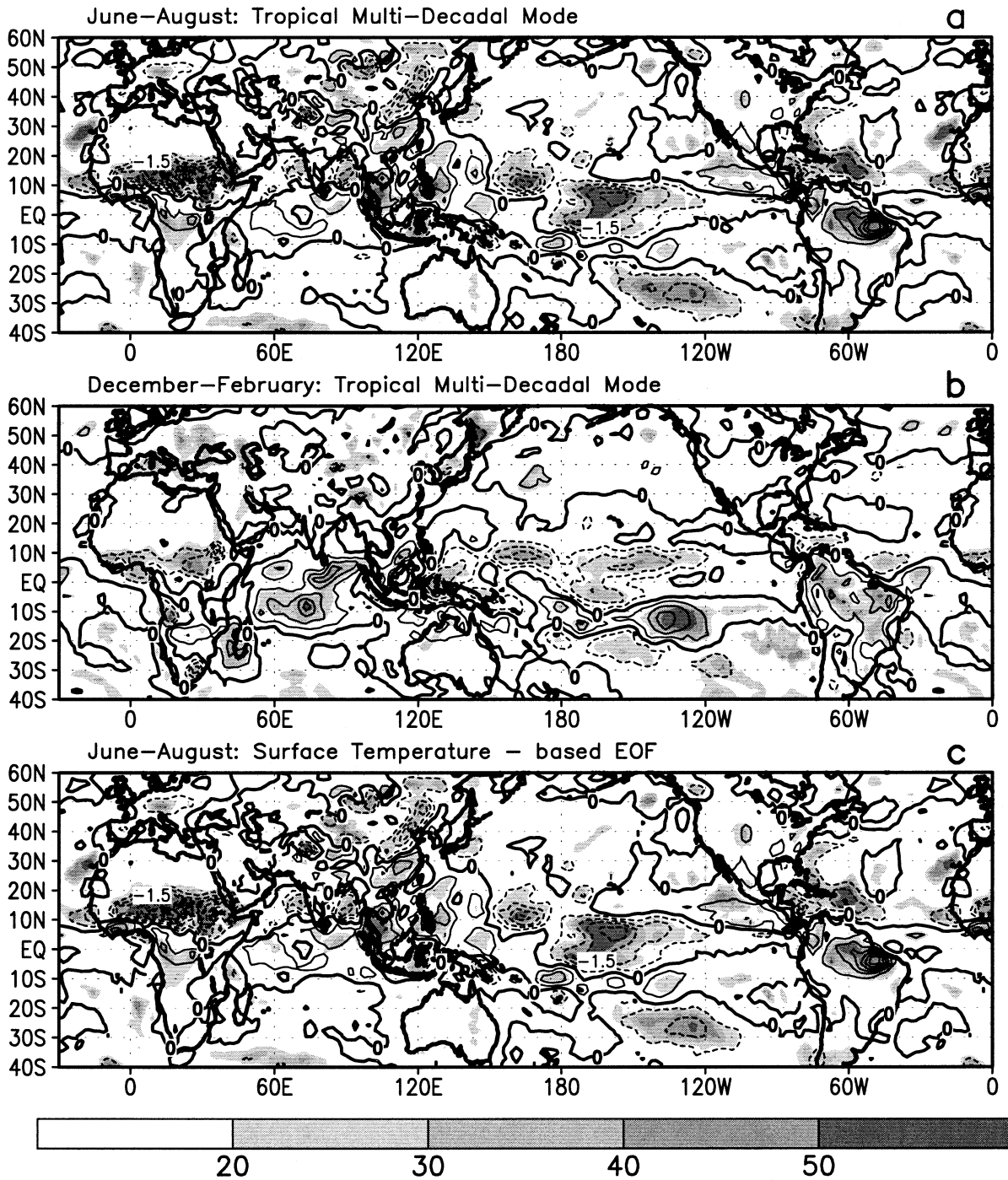## Regressed Anomalies and Explained Unfiltered Variance

FIG. 5. Tropical multidecadal mode regressed unfiltered seasonal precipitation rate anomalies (contours) and percent of explained unfiltered seasonal variance (shading) for (a) JJA and (b) DJF. (c) The corresponding fields associated with the leading surface temperature–based multidecadal EOF for JJA are also shown. Contour interval is 0.5 mm day^{-1} (std dev)$^{-1}$ of the mode.

Multi—Decadal EOF: Seasonal Precipitation Rate Regressed Anomalies and Explained LP—Filtered Variance
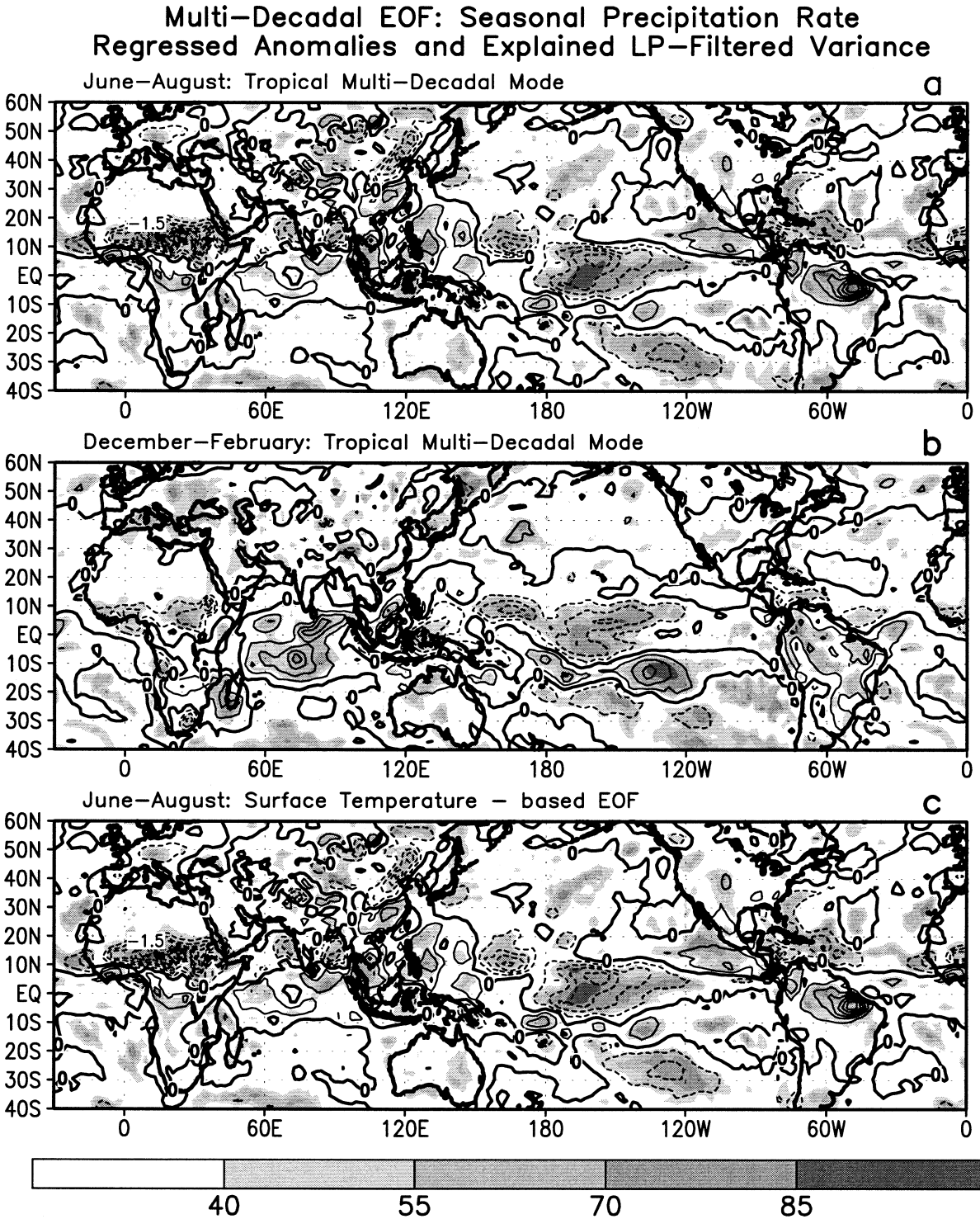

FIG. 6. Tropical multidecadal mode regressed 5-yr LP-filtered precipitation rate anomalies (contours) and percent of explained LP-filtered seasonal variance (shading) for (a) JJA and (b) DJF. (c) The corresponding fields associated with the leading surface temperature–based multidecadal EOF for JJA are shown. Contour interval is 0.5 mm day^{-1} (std dev)$^{-1}$ of the mode.

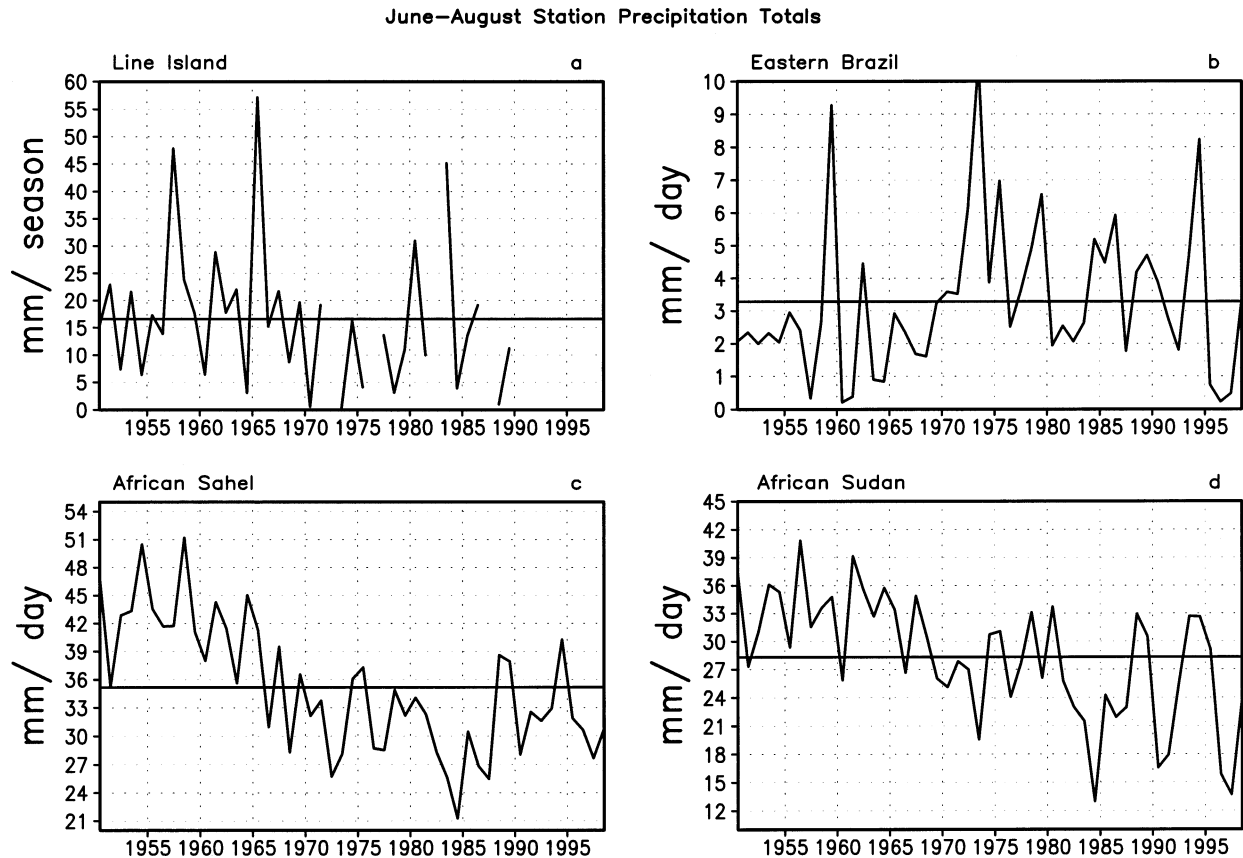**June–August Station Precipitation Totals**

FIG. 7. JJA observed seasonal rainfall: (a) Line Island station located in the central equatorial Pacific; area-averaged totals from Hulme (1995) over (b) eastern Brazil (5.5°–6.5°S, 45°–47°W), (c) the African Sahel (17.5°–12.5°N, 18°W–10°E), and (d) the African Sudan (12°–16°N, 32°–35°E).

motion is located over the central equatorial Pacific, with compensating subsidence over both the Indian Ocean and Amazon basin.

These core areas of velocity potential and precipitation anomalies are consistent with Chen et al. (2001, their Fig. 3), who calculated the difference in 200-hPa velocity potential for the DJF season between 1989–98 and 1958–77 and produced a strikingly similar pattern to the loadings for the tropical multidecadal mode. They related these differences to an "interdecadal change of the global divergent circulation" between the earlier and later decades, particularly over the Amazon basin, the tropical Pacific, and the Indian Ocean.

The loading centers and regions of explained variance between the tropical multidecadal and tropical interannual modes are approximately orthogonal (cf. Figs. 3c,d, and 4c,d). Also, the TMM accounts for 2–3 times the total unfiltered variance in the analysis region as the interannual mode. These results indicate that the two modes are largely distinct, and that possible low-frequency imprints onto the climate system by ENSO are not dominating the TMM. A similar finding for the leading multidecadal EOF of global SST anomalies is discussed by Mestas-Nuñez and Enfield (2001).

There is considerable independent data and published observational evidence to corroborate the rainfall variations associated with the tropical multidecadal mode. Over the central equatorial Pacific the indication of decreased rainfall during the 1980s–90s compared to the 1950s–60s is consistent with independent Line Island station data (Fig. 7a). Over the tropical North Pacific (10°) just west of the date line, and over the subtropical South Pacific (20°S) between the date line and 150°W, the indication of negative rainfall anomalies in recent decades is consistent with the downward trend in station rainfall totals and upward trend in OLR values described by Morrissey and Graham (1996, their Figs. 1, 2). Over the tropical South Pacific (along 10°S) the indication of above-average precipitation rates in recent decades is consistent with the upward trend in station rainfall totals and downward trend in OLR values shown by Morrissey and Graham.

Over the Amazon basin the indication of positive rainfall anomalies during the 1980s–90s is corroborated by the independent-gridded rainfall measurements of Hulme (1995) over eastern Brazil (Fig. 7b), an area with two to three reporting stations in almost every month since 1950. It is also consistent with Amazon basin

Multi—Decadal EOF: Seasonal Surface Temperatures
Regressed Anomalies and Explained Unfiltered Variance

June—August: Tropical Multi—Decadal Mode

December—February: Tropical Multi—decadal Mode

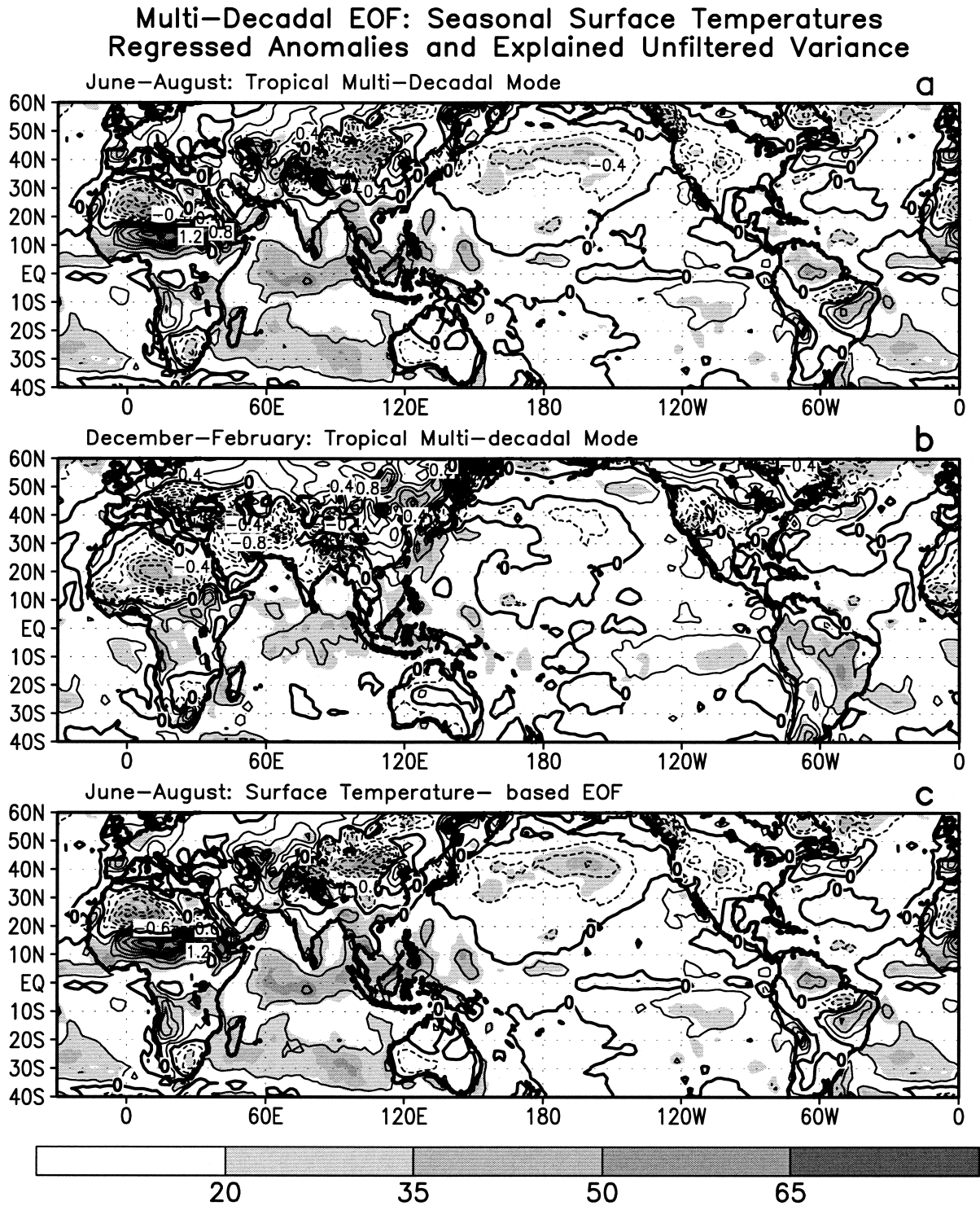June—August: Surface Temperature— based EOF

FIG. 8. Tropical multidecadal mode regressed surface temperature anomalies (contours) and percent of explained unfiltered seasonal variance (shading) for (a) JJA and (b) DJF. (c) The corresponding fields associated with the leading surface temperature–based multidecadal EOF for JJA are shown. Contour interval is 0.2°C (std dev)$^{-1}$ of the mode.

Multi—Decadal EOF: Seasonal Surface Temperatures
Regressed Anomalies and Explained LP—Filtered Variance

June—August: Tropical Multi—Decadal Mode

December—February: Tropical Multi—decadal Mode

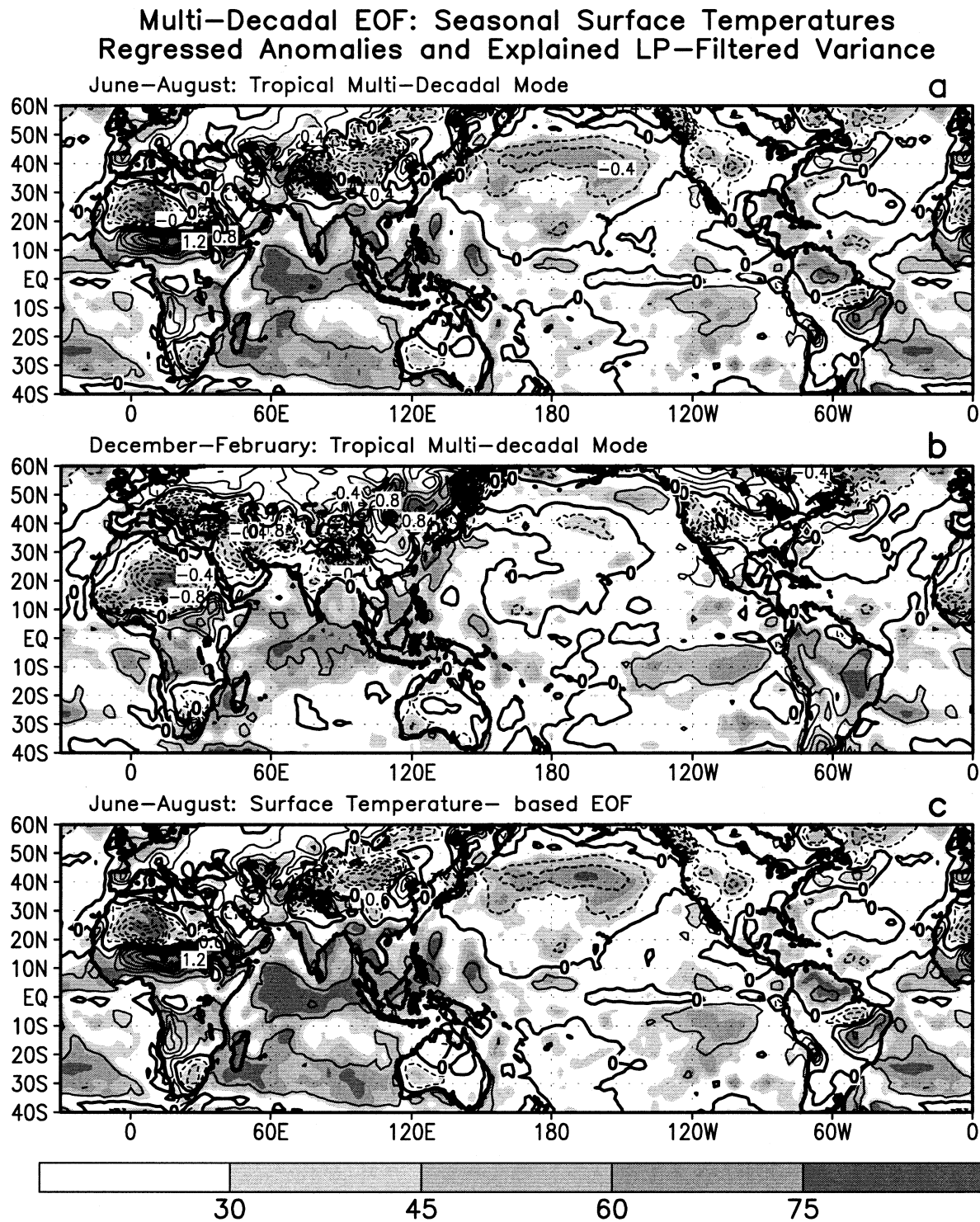June—August: Surface Temperature— based EOF

FIG. 9. Tropical multidecadal mode regressed 5-yr LP-filtered surface temperatures anomalies (contours) and percent of explained LP-filtered seasonal variance (shading) for (a) JJA and (b) DJF. (c) The corresponding fields associated with the leading surface temperature–based multidecadal EOF for JJA are shown. Contour interval is 0.2°C (std dev)$^{-1}$ of the mode.
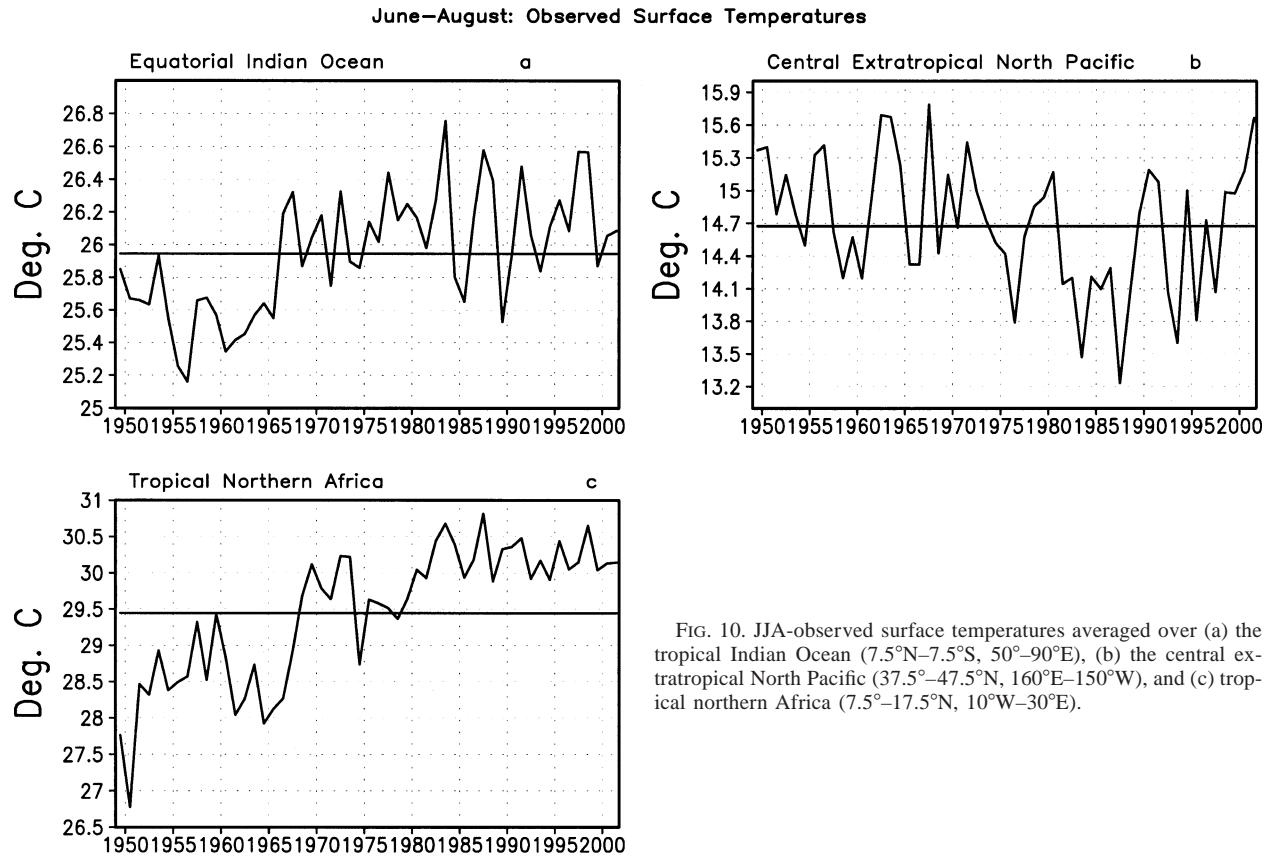
June–August: Observed Surface Temperatures

FIG. 10. JJA-observed surface temperatures averaged over (a) the tropical Indian Ocean (7.5°N–7.5°S, 50°–90°E), (b) the central extratropical North Pacific (37.5°–47.5°N, 160°E–150°W), and (c) tropical northern Africa (7.5°–17.5°N, 10°W–30°E).

rainfall variations described Chu et al. (1994) and Kumar et al. (1999), and by Chen et al. (2001) who noted increased rainfall and enhanced upper-level divergence over the Amazon basin in recent decades.

Over tropical northern Africa the indication of below-average JJA rainfall in recent decades is consistent with time series of area-averaged station rainfall totals in both the African Sahel (Fig. 7c), and the African Sudan (Fig. 7d), which show considerably more rain during the 1950s–60s compared to recent decades. These results are also consistent with numerous published analyses on West African monsoon rainfall variability (Shinoda 1990, 1995; Nicholson and Palao 1993; Rowell et al. 1995; Nicholson 1996; Ward 1998; Thaiw et al. 1998).

It has been suggested that a suppressed West African monsoon system is partly responsible for the below-average Atlantic hurricane activity observed during the 1970s through the mid-1990s (Gray 1990; Landsea and Gray 1992; Goldenberg and Shapiro 1996). The regressed negative rainfall rate anomalies during JJA across the tropical Atlantic, Caribbean Sea, and off of the east coast of the United States are consistent with this reduced hurricane activity (Fig. 5a).

c. Tropical multidecadal mode: Regressed surface temperature anomalies

The tropical multidecadal mode is associated with a Tropics-wide pattern of surface temperature anomalies

in both seasons, but notably excludes the entire east-central equatorial Pacific (contours, Fig. 8). The positive phase of the mode seen during the 1980s–90s is characterized by anomalous warmth in the Tropics, with the main warming extending from the Indian Ocean eastward across the tropical Pacific to the Amazon basin and tropical Northern Africa. It is also associated with generally below-average SSTs in the northern extratropics, particularly over the central North Pacific, and the high latitudes of the North Atlantic.

The TMM generally accounts for 35%–50% of the unfiltered seasonal surface temperature variance (shading, Figs. 8a,b) in these major anomaly regions, and for 60%–80% of the LP-filtered variance (shading, Figs. 9a,b). This signal is nearly identical to the spatial loadings calculated from the leading multidecadal EOF of seasonal tropical surface temperature anomalies (shown for JJA, Figs. 8c, 9c), and is also consistent with the leading multidecadal EOF of global sea surface temperatures presented by Mestas-Nuñez and Enfield (1999, 2001).

There is considerable observational evidence to substantiate the key surface temperature anomalies associated with the TMM. For example, the indicated warming of the tropical Indian Ocean (Fig. 10a) and cooling of the extratropical North Pacific (Fig. 10b) in recent decades is seen in the area-averaged SST anomalies

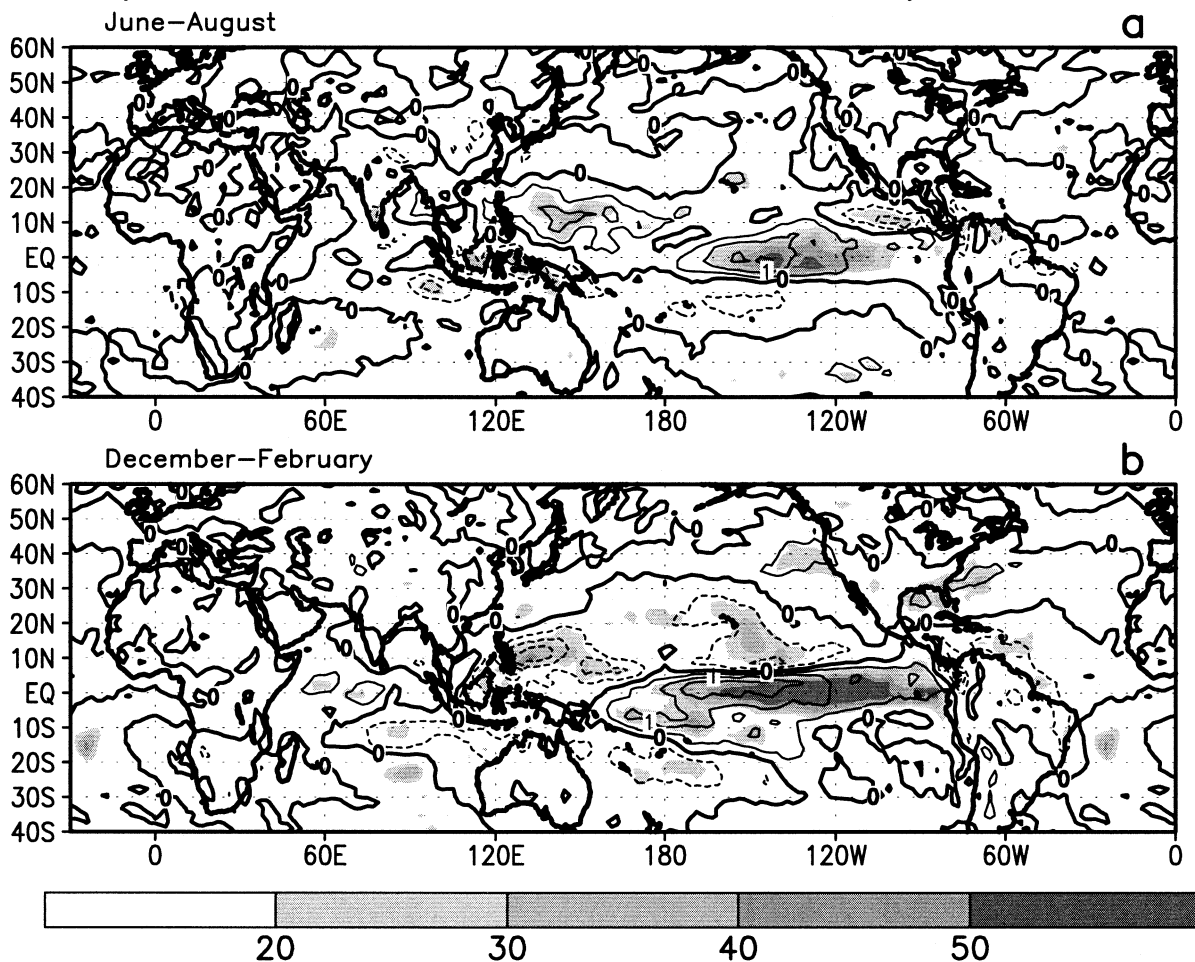## Tropical Interannual Mode Seasonal Precipitation Rates

FIG. 11. Tropical interannual (ENSO) mode regressed unfiltered seasonal precipitation rate anomalies (contours) and percent of explained unfiltered seasonal variance (shading) for (a) JJA and (b) DJF. Contour interval is 0.5 mm day^{-1} (std dev)$^{-1}$ of the mode.

calculated from the Smith et al. (1996) dataset. These results are consistent with known fluctuations in the PDO (Mantua et al. 1997), with the strongest relationship between the TMM and PDO seen during JJA (Fig. 9a), rather than DJF (Fig. 9b). They are also consistent with the known inverse relationship in SST variations occurring on decadal time scales between the Indian Ocean and the extratropical North Pacific (Kawamura 1994).

Hoerling et al. (2001) indicate that the overall warming trend over the combined tropical Indian and tropical Pacific Oceans might act to force a cooling of the North Atlantic at both high latitudes and in the Tropics, similar to that indicated by the positive phase of the TMM. Multidecadal SST fluctuations in these key regions of the North Atlantic are referred to as the Atlantic multidecadal mode (Mestas-Nuñez and Enfield 1999). The levels of explained SST variance by the TMM in these core areas are comparable to those of the Atlantic multidecadal mode itself (Mestas-Nuñez and Enfield 1999).

Over subtropical northern Africa the indicated dipole in regressed surface temperature anomalies associated with the TMM is consistent with a sharp rise in surface temperatures in the African Sahel during the drought-stricken decades of the 1970s to the early 1990s (Fig. 10c). Interestingly, we find that if land surface temperature anomalies are neglected, the spatial correlations between the regressed surface temperature and precipitation rate anomalies and those associated with the tropical multidecadal mode drop from 0.96 to approximately 0.7. This result highlights the important relationship between land surface temperatures and tropical convection, and is especially pertinent to the African Sahel and Sudan regions where a strong link is evident between multidecadal variations in land surface temperatures and the strength of the West African monsoon (Charney et al. 1975; Xue and Shukla 1993; Zeng et al. 1999; Zeng and Neelin 2000).

During DJF the positive phase of the TMM also captures the observed cooling in surface temperatures over

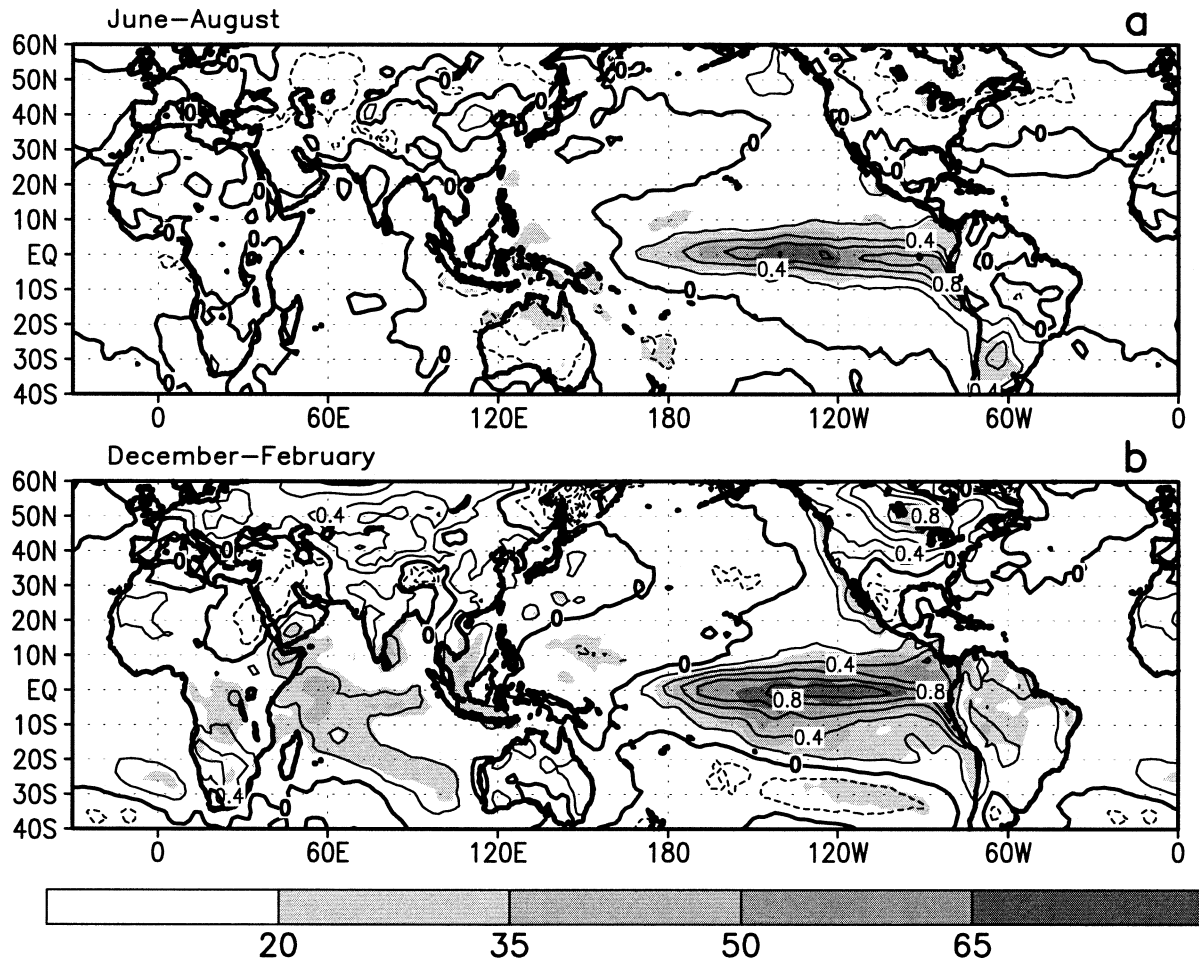## Tropical Interannual Mode: Seasonal Surface Temperatures

FIG. 12. Tropical interannual (ENSO) mode regressed unfiltered seasonal surface temperatures anomalies (contours) and percent of explained unfiltered seasonal variance (shading) for (a) JJA and (b) DJF. Contour interval is 0.2°C (std dev)$^{-1}$ of the mode.

the western United States during the 1980s–90s, along with a concurrent warming throughout Canada and the eastern United States, as documented by Livezey and Smith (1999). Over Europe it captures warmer temperatures to the north and west and cooler temperatures to the south and east.

d. Tropical interannual (ENSO) mode: Velocity potential, precipitation rate, and surface temperature

The tropical interannual (ENSO) mode accounts for more than 60% of the unfiltered variance in seasonal 200-hPa velocity potential anomalies over the eastern half of the Pacific Ocean in both seasons, and for 40%–60% of the unfiltered variance over the eastern Indian Ocean during JJA (shading, Fig. 3d), and across Indonesia during DJF (shading, Fig. 4d). This mode also accounts for more than 80% of the total interannual

velocity potential variance in the above regions during both seasons (not shown).

The positive phase of the ENSO mode captures El Niño, and features anomalous upper-level divergence (Figs. 3d, 4d) and above-average precipitation rates across the central and east-central equatorial Pacific in both seasons (Figs. 11a,b). It also features anomalous upper-level convergence and below-average precipitation rates over Indonesia. These conditions reflect a reduced strength of the equatorial Walker circulation, and an enhanced thermally direct circulation over the central equatorial Pacific, typical of El Niño (Gill 1982; Rasmusson and Carpenter 1982; Wright et al. 1988). This link to El Niño is evident in the positive sea surface temperature anomalies over the eastern half of the equatorial Pacific (Fig. 12), where more than 65% of the unfiltered seasonal SST variance is accounted for by the mode. Conversely, the tropical multidecadal mode exhibits no significant SST loadings over the eastern half
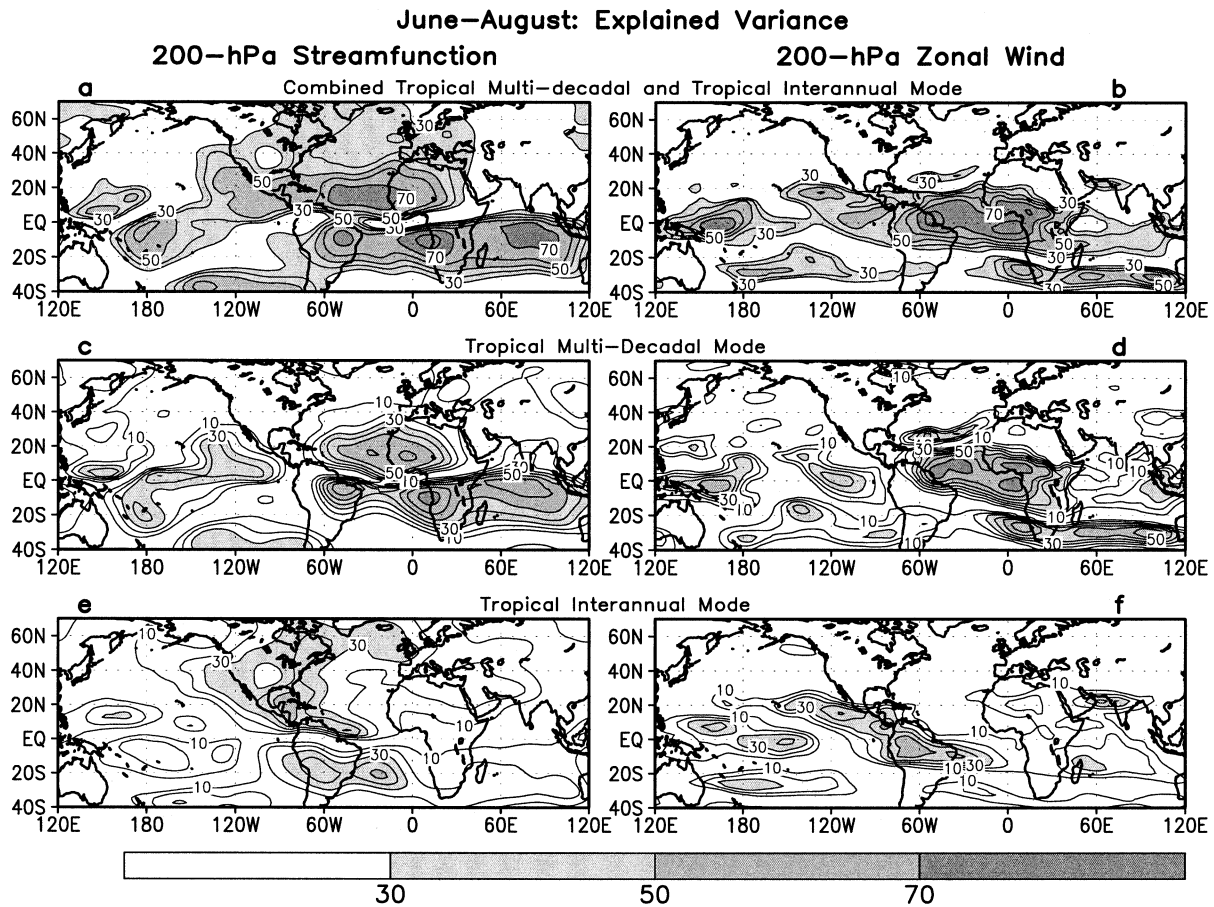
FIG. 13. 200 hPa: JJA percent of explained variance of the (left) unfiltered seasonal streamfunction and (right) zonal wind anomalies associated with (a), (b) the combined tropical multidecadal mode (TMM) and ENSO; (c), (d) the TMM; and (e), (f) ENSO.

of the equatorial Pacific, again suggesting that it is distinct from ENSO.

5. Regression of leading tropical modes onto 200-hPa streamfunction winds

a. JJA: 200 hPa

During JJA the tropical multidecadal mode and ENSO together account for a significant fraction of the unfiltered seasonal variance in 200-hPa streamfunction and zonal wind anomalies throughout the Tropics and subtropics of both hemispheres (Figs. 13a,b), with 30%–50% of the variance explained over the Pacific Ocean (Figs. 13c,d and 11e,f), and more than 70% of the variance explained over the Atlantic Ocean, Africa, and the Americas. The TMM accounts for most of the signal over the eastern Atlantic Ocean and Africa (Figs. 13c,d), and ENSO accounts for more of the signal over the Americas (Figs. 13e,f).

Both modes exhibit an approximate zonal wavenumber-1 pattern of regressed 200-hPa streamfunction anomalies in the subtropics of both hemispheres (Figs. 14a,b), with a pronounced interhemispheric symmetry

to the anomalies evident. This symmetry is a signature response of the upper-level atmospheric circulation to anomalous tropical convection.

The positive phase of the TMM seen during the 1980s–90s is associated with anticyclonic streamfunction anomalies over the eastern Pacific and cyclonic anomalies across the Atlantic Ocean and Africa (Fig. 14a). This anomaly pattern is approximately opposite in sign to the climatological mean zonal wave pattern (Fig. 14c), indicating an overall weaker 200-hPa circulation in the Tropics, especially across the Atlantic Ocean and Africa where upper-level westerly anomalies reflect a below-average strength of the tropical easterly jet (cf. Figs. 14a,d).

A major component of the tropical multidecadal mode during JJA is the West African monsoon variability. The positive phase of the TMM is associated with a suppressed West African monsoon system, as indicated by anomalous upper-level convergence (light shading, Fig. 14a) and below-average precipitation rates in that region. The correspondingly reduced divergent outflow from tropical northern Africa is then consistent with a reduction in upper-level convergence and compensating
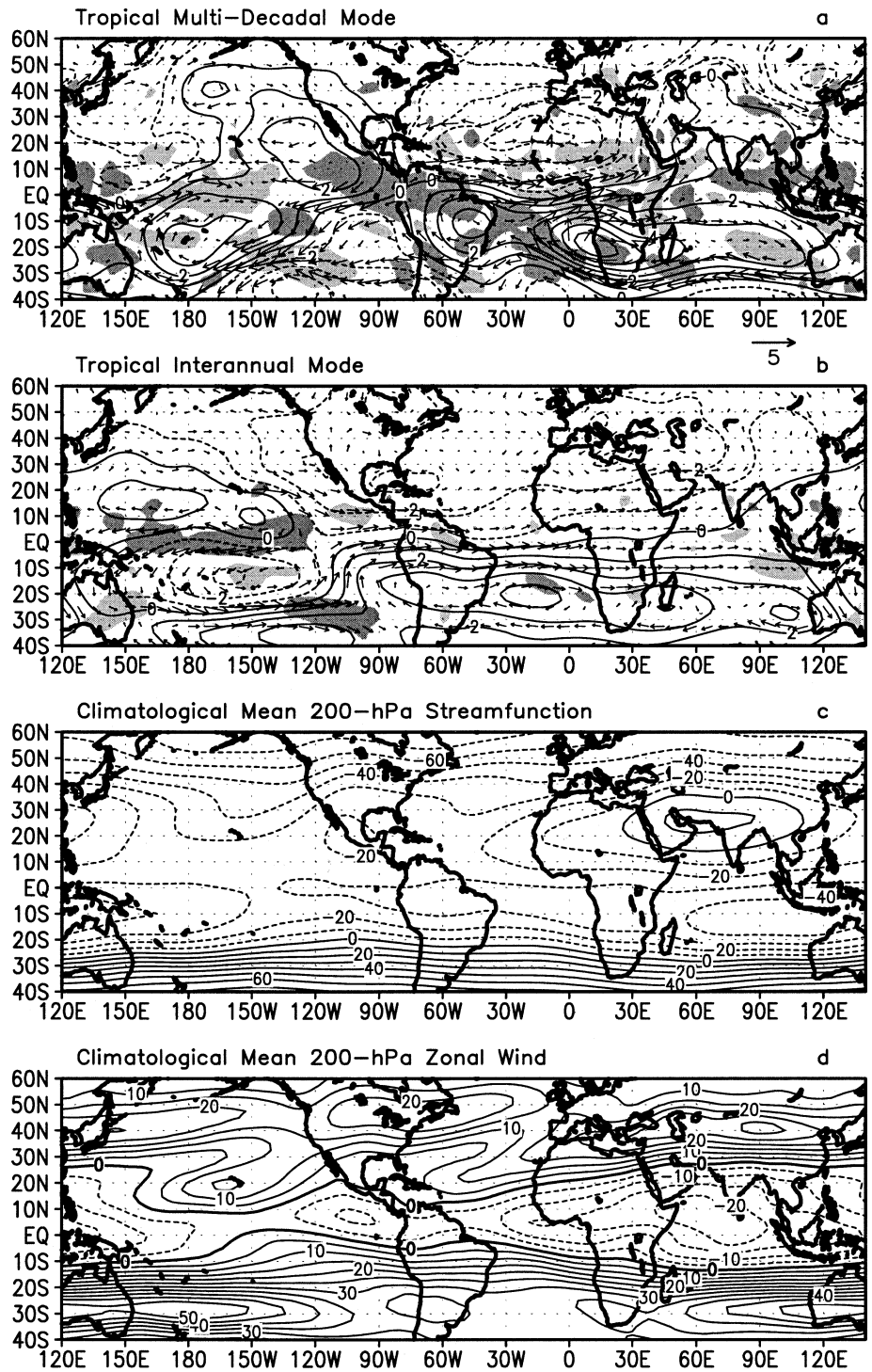
June–August: 200–hPa Circulation

FIG. 14. JJA regressed seasonal anomalies of 200-hPa streamfunction (contours), divergence (shading), and total vector wind associated with (a) the TMM and (b) the tropical interannual (ENSO) mode. Contour interval for streamfunction is 1×10^6 m^2 s^{-1} (std dev)$^{-1}$ of the mode. Divergence (convergence) anomalies exceeding 4×10^{-7} s^{-1} (std dev)$^{-1}$ of the mode are shaded dark (light). The vector wind anomalies have units of m s^{-1} (std dev)$^{-1}$ of the mode, with the wind scale located above (b). (c), (d) 1951–2000 mean streamfunction and zonal wind, with contour intervals of 10×10^6 m^2 s^{-1} and 5 m s^{-1}, respectively.

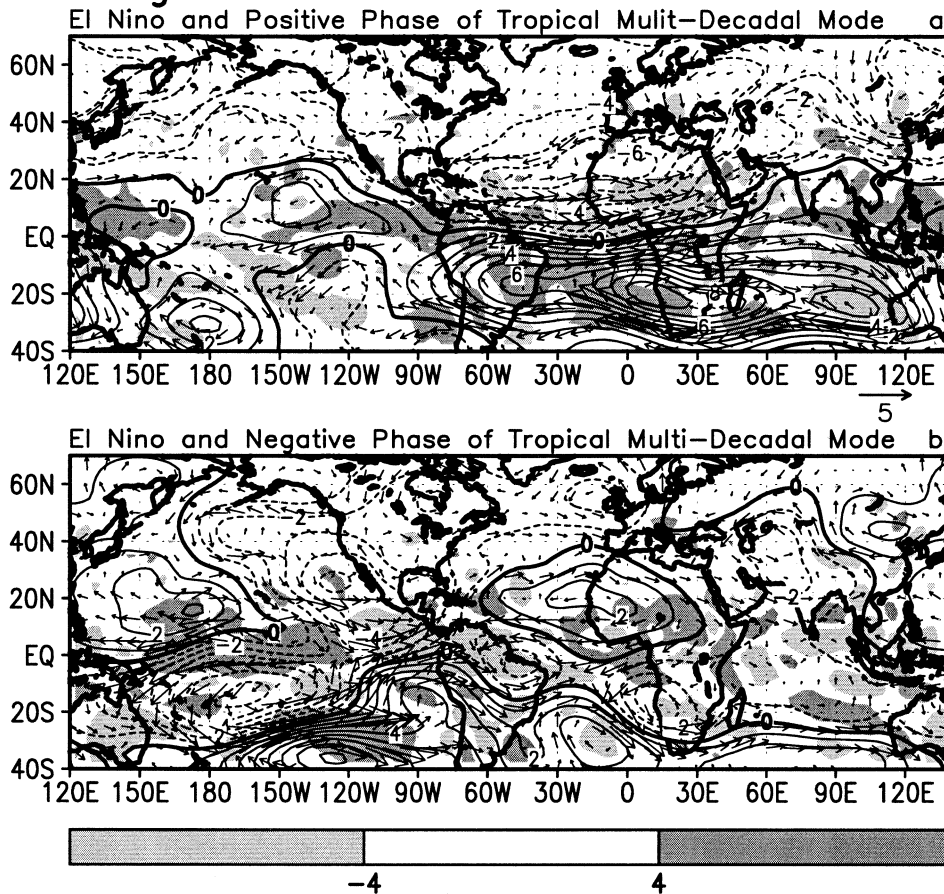## June–August Combined Modes: 200–hPa Circulation

FIG. 15. JJA regressed seasonal anomalies of 200-hPa streamfunction (contours), divergence (shading), and total vector wind associated with a +1.0 std dev of the tropical interannual (ENSO) mode combined with the (a) +1.0 std dev and (b) −1.0 std dev of the tropical multidecadal mode. Contour interval for streamfunction is 1×10^6 m^2 s^{-1} (std dev)$^{-1}$ of the modes. Divergence (convergence) anomalies exceeding 4×10^{-7} s^{-1} (std dev)$^{-1}$ of the modes are shaded dark (light). The vector wind anomalies have units of m s^{-1} (std dev)$^{-1}$ of the mode, with wind scale located above (b).

subsidence in the vicinity of the mean subtropical ridge axis across the South Atlantic and southern Africa (recall Fig. 3c). These conditions are then consistent with a below-average strength of the upper-level ridge in those regions, which completes the interhemispheric symmetry with the anomalously weak subtropical ridges across the North Atlantic and northern Africa.

For El Niño, the appearance of anticyclonic anomalies over the Pacific sector and cyclonic anomalies over the Americas and the Atlantic Ocean during JJA is consistent with classical interpretations of ENSO (Mo and Kousky 1993). For the linear combination of the two tropical modes, the strongest signal in the Tropics and subtropics is found when their PC time series are in phase (Fig. 15a), and the weakest signal is found when they are out of phase (Fig. 15b). This result suggests stronger El Niño teleconnections during the positive phase of the TMM, and stronger La Niña teleconnections during the negative phase of the TMM. These results are consistent with the strong multidecadal mod-

ulations of the ENSO teleconnections discussed by Gershunov and Barnett (1998). They may help to explain the tendency for stronger El Niño episodes during the 1980s–90s compared to the 1950s–60s (see section 4a and Figs. 3a, 4a).

b. DJF: 200 hPa

During DJF the combined tropical multidecadal mode and ENSO again account for a significant fraction (30%–50%) of the unfiltered seasonal variance in 200-hPa streamfunction and zonal wind anomalies throughout the Tropics and subtropics of both hemispheres and over the extratropical North Atlantic (Figs. 16a,b). The regional maxima in explained variance associated with the TMM are lower (10%–30%) during DJF (Figs. 16c,d) compared to JJA (50%–70%), while those of the interannual mode are higher during DJF (Figs. 16e,f). These results are consistent with the lack of significant West African monsoon variability during DJF, combined

December–February: Explained Variance
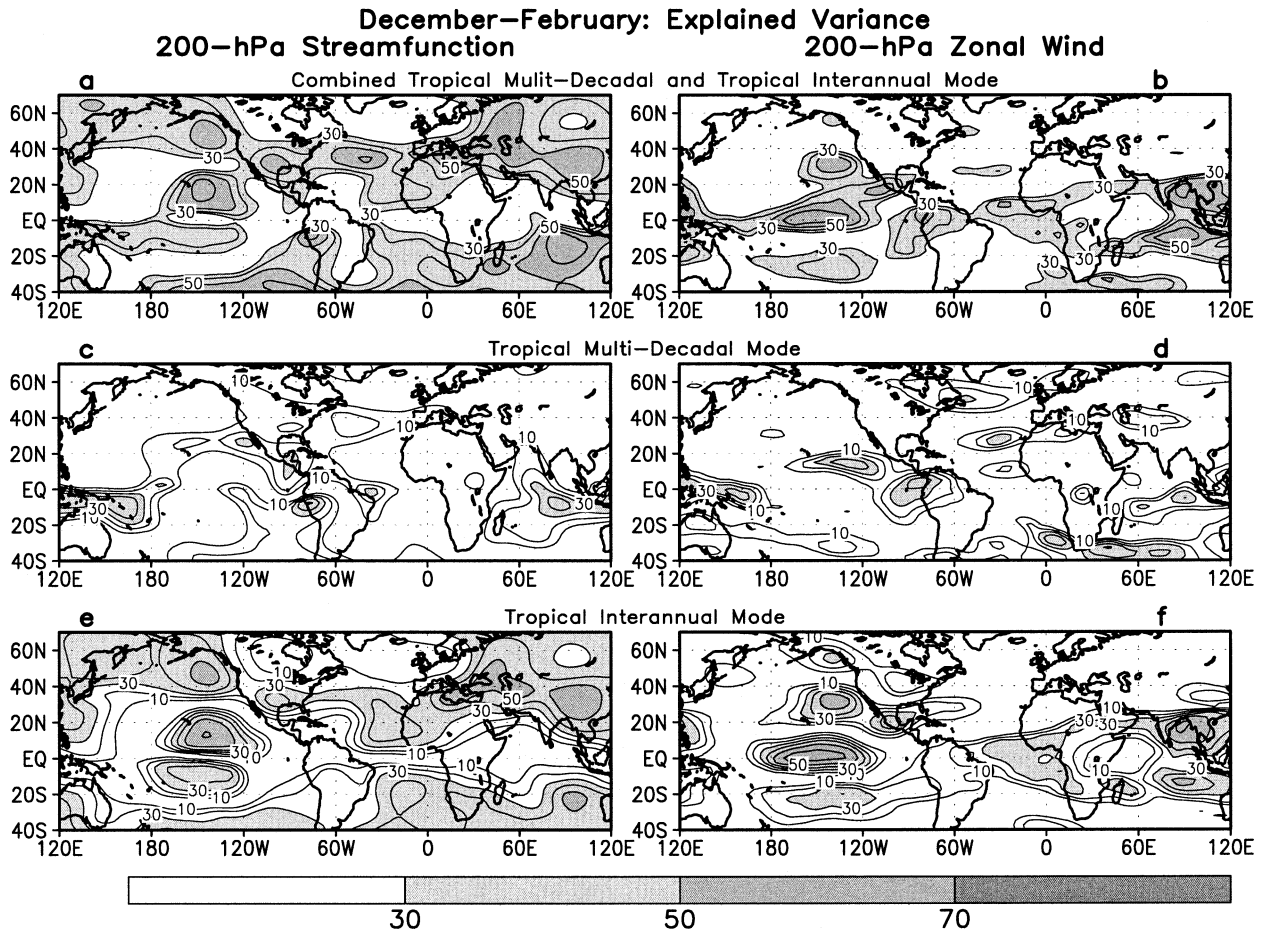#### 200–hPa Streamfunction   200–hPa Zonal Wind

FIG. 16. As in Fig. 13, except for DJF.

with the overall peak in the ENSO cycle typically observed during this season.

Regressions of the PC time series onto the 5-yr running mean LP-filtered anomalies show that the TMM accounts for more than 50% of the multidecadal variance in the 200-hPa streamfunction and zonal wind across the eastern Pacific and the Americas in each hemisphere, and across the North Atlantic in key regions of the NAO (Figs. 17a,b). These results suggest a potentially large modulating influence of the ENSO teleconnections (Figs. 17c,d) by the TMM.

Over the North Pacific the positive phase of the TMM (Fig. 18a) is associated with anticyclonic circulation anomalies over the subtropical eastern Pacific in both hemispheres, indicating an eastward extension of the subtropical ridges normally centered over the western Pacific (Fig. 18c). Upper-level westerly anomalies along the poleward flank of the anomalous subtropical ridge indicate an eastward extension of the east Asian jet stream (Fig. 18d). Similar structural changes in the subtropical ridge and east Asian jet stream are seen during El Niño (Fig. 18b). As a result, the strongest signal is again found when the PC time series of the two tropical

modes are in phase (Fig. 19a), and the weakest signal is found when they are out of phase (Fig. 19b).

To better quantify this result the regressed area-averaged 200-hPa streamfunction and zonal wind anomalies (Figs. 20a,b, respectively) over the North Pacific are shown for various linear combinations of the standardized mode amplitudes. In these figures the standardized amplitudes of ENSO (TMM) are shown on the vertical (horizontal) axis. The regressed anomaly for each combination of the modes is plotted, and the entire set of regressed anomalies is then contoured. The general horizontal slope to the contours in both panels is consistent with the strong ENSO influence on these parameters. However, the multidecadal signal is seen to substantially influence the ENSO teleconnections, especially during weak-to-moderate ENSO episodes.

A second issue of interest is the possible relationship between multidecadal variations in anomalous tropical forcing and the wintertime NAO (Hoerling et al. 2001). Our analysis indicates that the PC time series of the TMM is in phase with the known multidecadal fluctuations in the NAO (Halpert and Bell 1997), with the negative phase of the NAO observed during the 1950s–

December–February
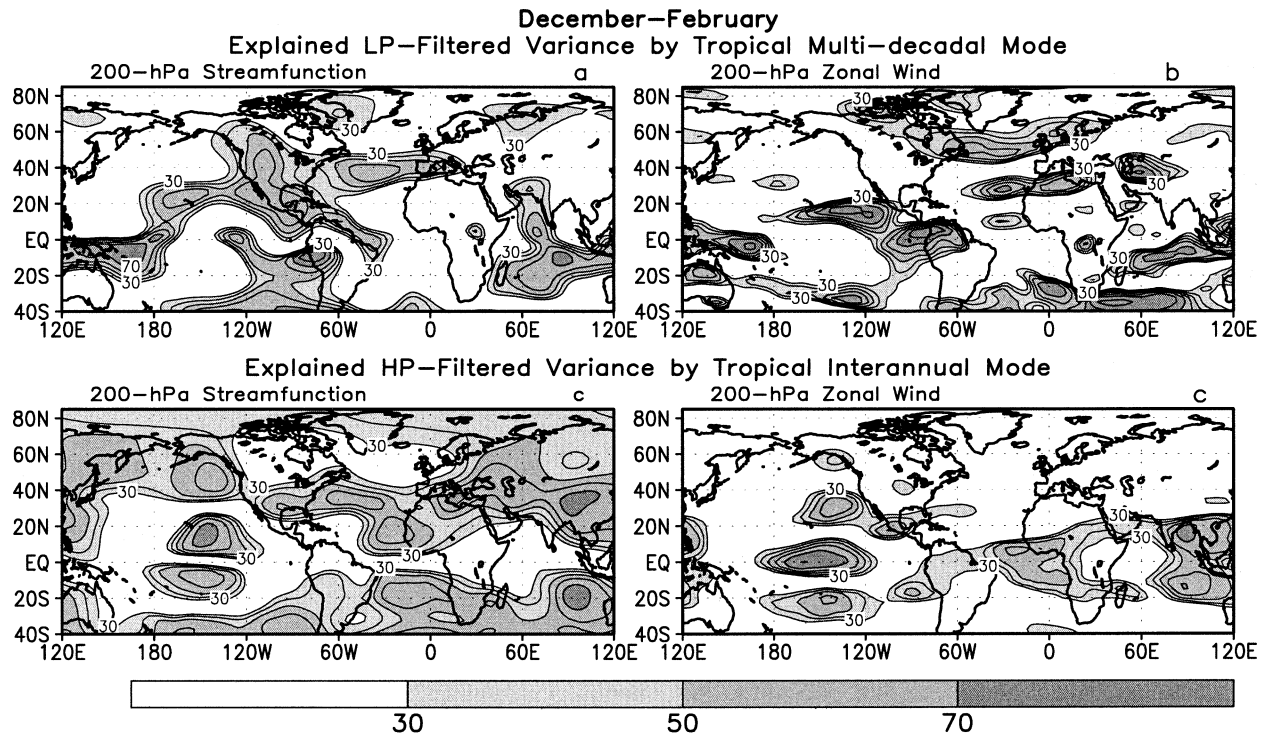### Explained LP–Filtered Variance by Tropical Multi–decadal Mode

FIG. 17. DJF percent of explained variance of the (a), (b) 5-yr LP-filtered seasonal anomalies of (left) 200-hPa streamfunction and (right) zonal wind by the tropical multidecadal mode, and (c), (d) 5-yr high-pass-filtered seasonal anomalies by the tropical interannual (ENSO) mode.

60s and the positive phase observed during the 1980s–90s.

The TMM captures all key structural aspects of the NAO (Fig. 18a). For the positive phase, these include an anomalously strong Icelandic low, an amplified ridge extending from the eastern United States to central Europe, increased westerlies extending from eastern Canada to England, and anomalous upper-level confluent flow over eastern Canada within the entrance region of the anomalous North Atlantic jet stream. Looking farther west it is seen that this anomalous confluent flow is associated with a larger-scale circulation pattern over North America, characterized by a stronger mean ridge in the west and a weaker mean trough in the east.

At lower latitudes one finds reduced westerlies along the entire southern flank of the subtropical jet stream, which extends from east of Hawaii to the eastern United States and eventually merges with the North Atlantic jet stream. The associated anomalous anticyclonic circulation overspreads not only the entire southern flank of the subtropical jet stream, but also extends eastward over the central North Atlantic consistent with the positive phase of the NAO. Also consistent with the NAO, the positive phase of the TMM captures the anomalous warmth observed across northern Europe, Canada, and the eastern United States in recent decades (Hurrell 1998), along with the cool phase of the Atlantic multidecadal mode (recall Fig. 9a).

The main ENSO influence on the NAO is found over the southern United States and central North Atlantic (Figs. 17c,d). El Niño favors a negative phase of the NAO by contributing to cyclonic streamfunction anomalies in these regions (Fig. 18b), while La Niña favors a positive NAO.

The regressed seasonal NAO index is shown for various linear combinations of the standardized TMM and ENSO (Fig. 20c). The strongest regressed NAO index is seen when the two tropical modes are out of phase (Fig. 19b). When the multidecadal signal is strong, it dominates ENSO in all but the strongest cases. Corresponding regressions onto the seasonal Atlantic multidecadal mode index shows the dominant influence of the TMM (Fig. 20d).

c. JJA and DJF: 850 hPa

In both seasons the combined leading tropical modes account for more than 70% of the unfiltered variance in seasonal 850-hPa zonal wind anomalies over the central and east-central equatorial Pacific (Figs. 21a,b). The TMM accounts for most of the signal in the east (Figs. 21c,d) and ENSO accounts for most of the signal in central and west (Figs. 21e,f). The combined modes also account for 30%–50% of the unfiltered seasonal variance over the tropical Atlantic in both seasons, and for 50%–70% of the variance over tropical northern Africa
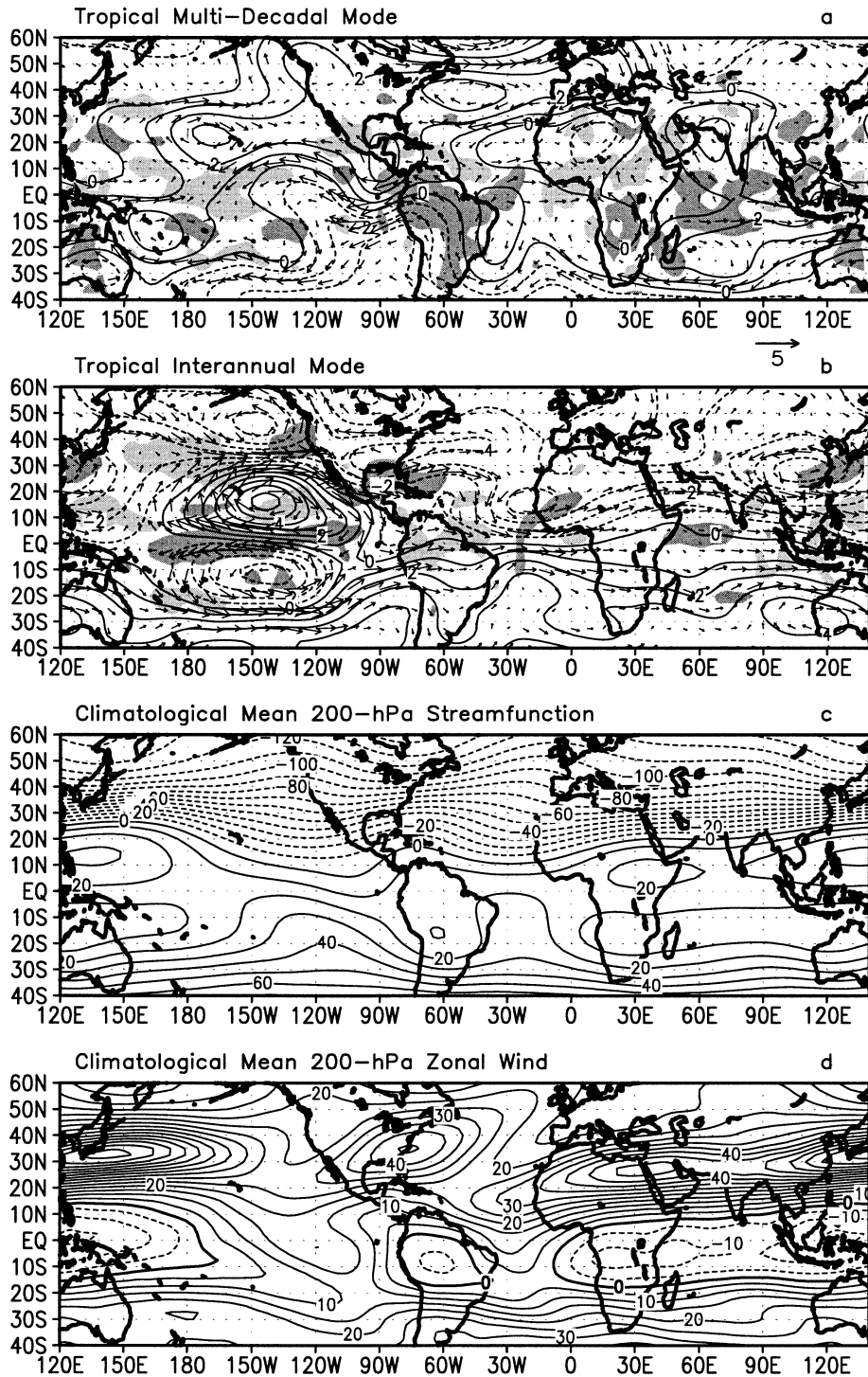
December−February: 200−hPa Circulation

FIG. 18. As in Fig. 14, except for DJF.

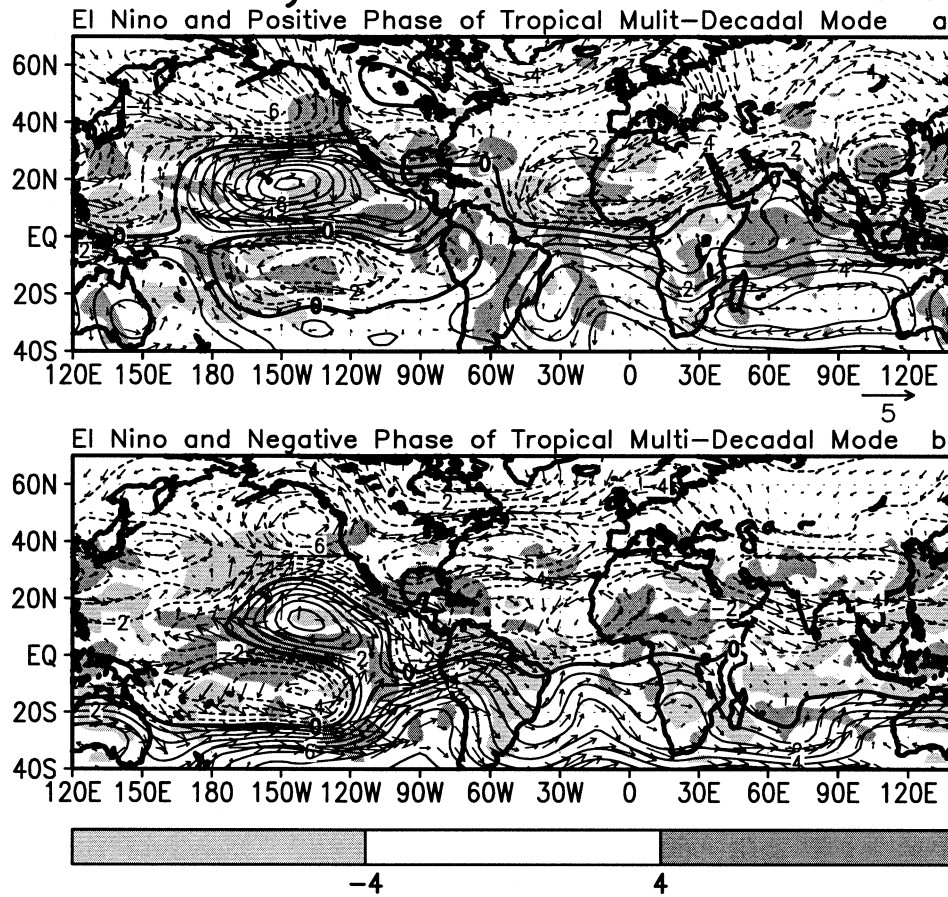## December–February Combined Modes: 200–hPa Circulation

FIG. 19. As in Fig. 15, except for DJF.

in JJA. Much of the signal across the eastern tropical Atlantic and Africa is associated with the TMM.

For both modes the 850-hPa zonal wind anomalies over the tropical Pacific are generally opposite in sign to their 200-hPa counterparts, which is consistent with the baroclinic response of the tropical atmosphere to large-scale convective anomalies (Bjerknes 1969; Gill 1982). The TMM also features a reversal in sign of the upper- and lower-level zonal wind anomalies over the tropical Atlantic and Africa, which is consistent with the baroclinic response to anomalous tropical convection in both the West African monsoon region and the Amazon basin. These indications are consistent with time series of station radiosonde winds over tropical northern Africa during JJA at both 200 (Fig. 22a) and 850 (Fig. 22b) hPa.

6. Summary

1) The TMM is identified and shown to be the dominant multidecadal mode of tropical convective precipitation and surface temperatures variability in the NCEP–NCAR reanalysis during JJA and DJF.
2) This mode provides a global-scale perspective on many known aspects of decadal climate variability, and relates this variability to coherent fluctuations in tropical convection and surface temperatures in the core regions of the West African monsoon, the central tropical Pacific, the Amazon basin, and the tropical Indian Ocean.
3) Specifically, the TMM captures the global climate regimes observed during the 1950s–60s and 1980s–90s, and the 1970s transition between these climate regimes.
4) Although the PC time series of the TMM can be approximated by an overall upward trend during the 52-yr (1949–2000) analysis period, this characterization can be misleading because the upward trend is seen mainly only during the 1970s.
5) We find that the spatial and temporal characteristics of the TMM are distinct from those associated with ENSO.
6) In the Tropics and subtropics the regressed seasonal anomalies are stronger and more spatially extensive when the PC time series of the TMM and ENSO are in phase. Stronger El Niño (La Niña) teleconnections are indicated for the positive (negative) phase of the TMM seen during the 1980s–90s (1950s–60s).
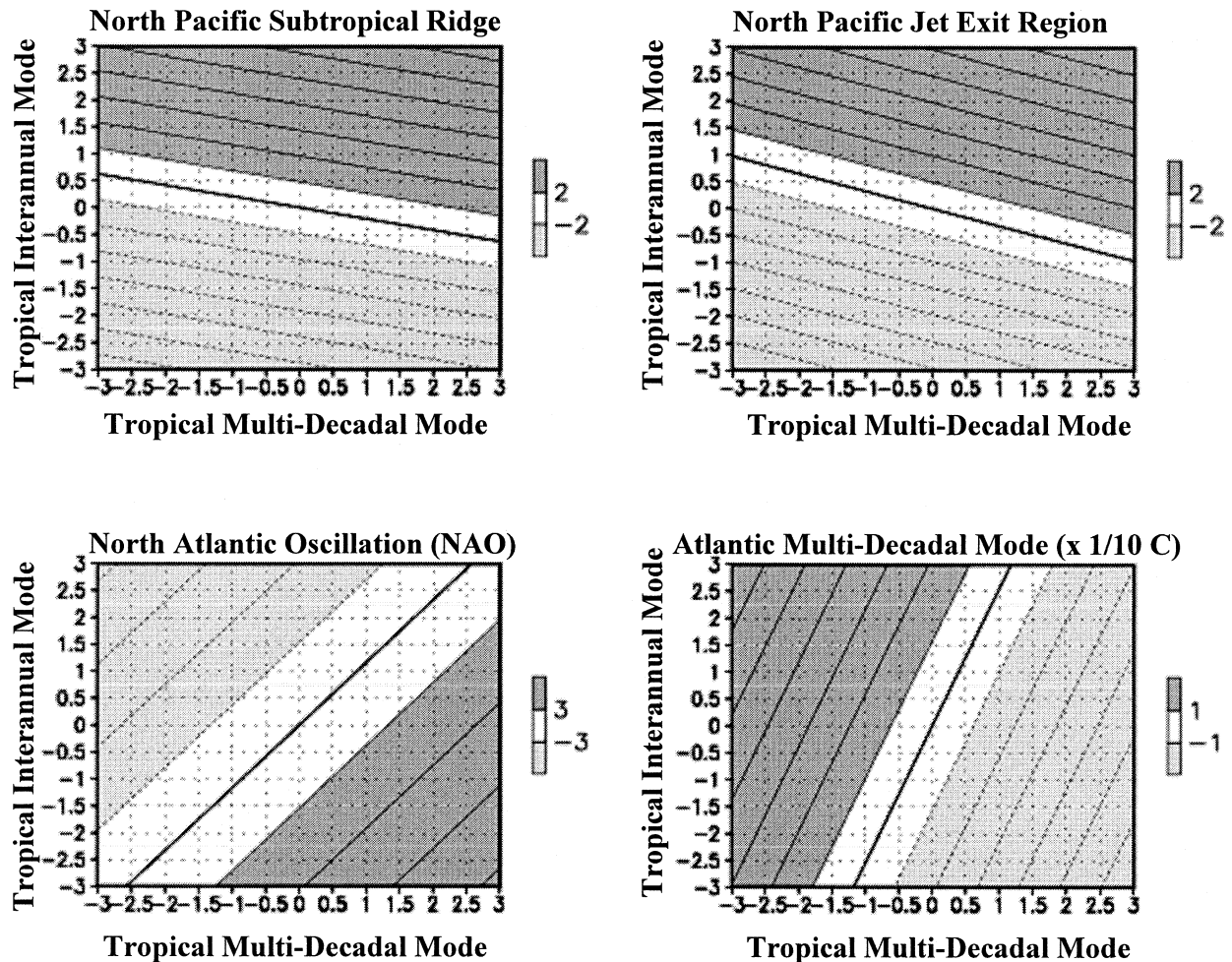
FIG. 20. DJF regression of area-averaged unfiltered seasonal anomalies onto standardized strengths of the tropical interannual (ENSO) mode (vertical axis) and tropical multidecadal mode (horizontal axis): 200-hPa streamfunction anomalies in (a) the North Pacific subtropical ridge region (5°–20°N, 160°–110°W) and (c) the core areas of the NAO; (b) 200-hPa zonal wind anomalies in the east Asian jet exit region (25°–35°N, 180°–120°W); (d) SST anomalies in the core areas of the Atlantic multidecadal mode. The NAO and Atlantic multidecadal mode values are proxy regression indices for these modes. The NAO index represents the regressed difference (south − north) in area-weighted 200-hPa streamfunction anomalies between the south (30°–50°N, 90°W–0°) and north (65°–80°N, 90°W–0°). The Atlantic multidecadal mode index represents the difference (north − south) in the regressed area-weighted SST anomalies between the north (50°–60°N, 60°–10°W) and south (5°–15°N, 80°–20°W).

7) The TMM captures all key structural aspects of the NAO, thus, linking climate fluctuations in the global Tropics to multidecadal variations in the NAO. The PC time series of the TMM varies in phase with the NAO index. The strongest regressed seasonal NAO index occurs when the TMM and ENSO are out of phase.

7. Discussion

The leading multidecadal mode in the global Tropics (30°N–30°S) has been isolated for the December–February (DJF) and June–August (JJA) seasons based on EOF analyses of seasonal tropical convective rainfall variability and tropical surface (land + ocean) temperature variability. G. D. Bell and M. Chelliah (2004,

unpublished manuscript) show that the tropical multidecadal mode (TMM) for the August–October season is similar to that for JJA. Because of the phenomenological nature of this study, one cannot attribute a cause(s) of this multidecadal variability from our results.

The TMM captures the global climate regimes observed during the 1950s–60s and 1980s–90s, and the 1970s transition between these climate regimes. It provides a global-scale perspective on decadal climate variability by relating these climate regimes to coherent multidecadal variations in tropical convection and surface temperatures in four core regions: the West African monsoon region, the central tropical Pacific, the Amazon basin, and the tropical Indian Ocean.

The TMM incorporates many aspects of decadal climate variability already addressed in the literature, in-

850-hPa Winds
Combined Tropical Multi-Decadal and Tropical Interannual Mode

Tropical Multi-Decadal Mode
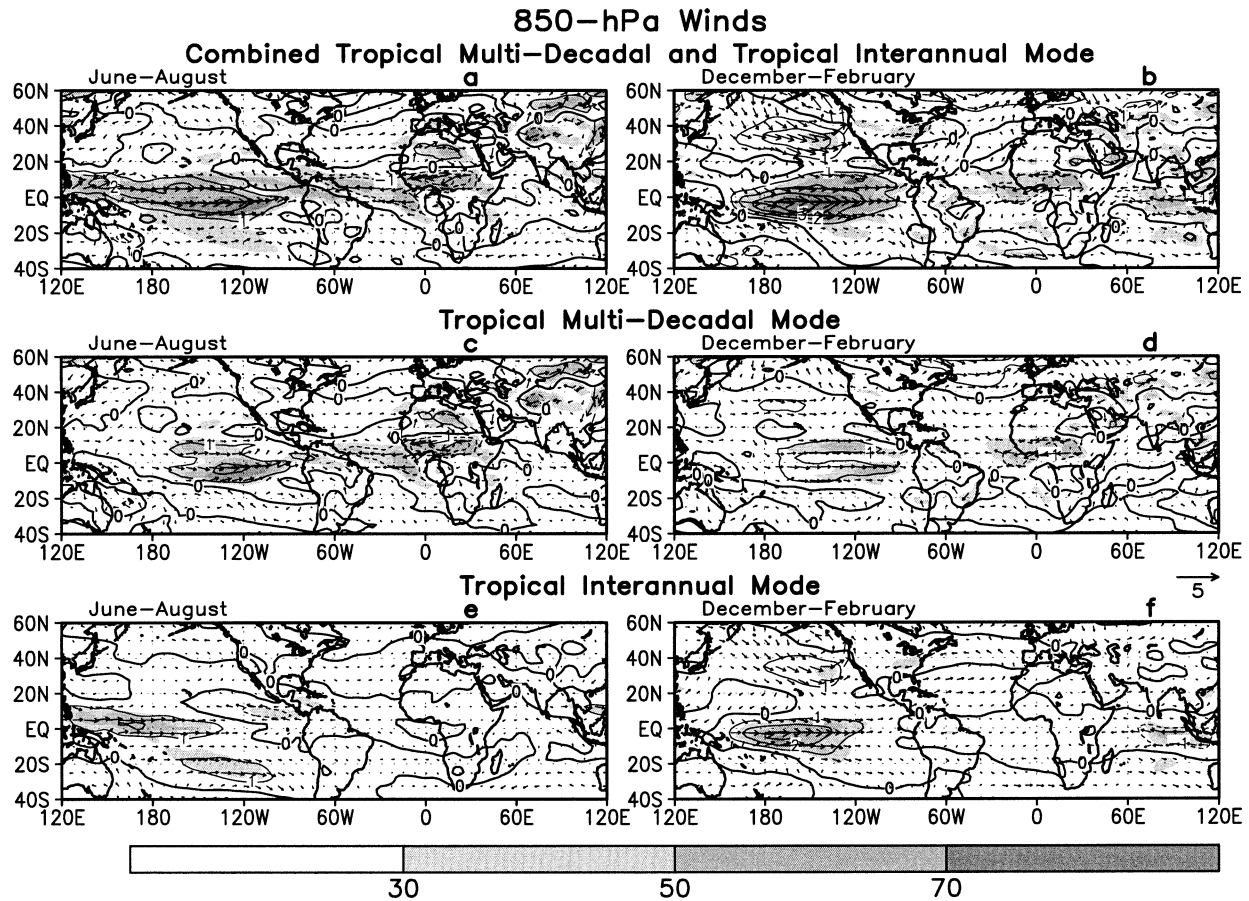
Tropical Interannual Mode

FIG. 21. 850-hPa: Regressed unfiltered seasonal vector wind and zonal wind speed anomalies (contours) and percent of explained variance of the unfiltered seasonal zonal wind anomalies (shading), during (left) JJA and (right) DJF associated with (a), (b) the combined TMM and ENSO; (c), (d) the TMM; and (e), (f) ENSO. Units are m s^{-1} (std dev)$^{-1}$ of the mode, with vector scale located above (f).
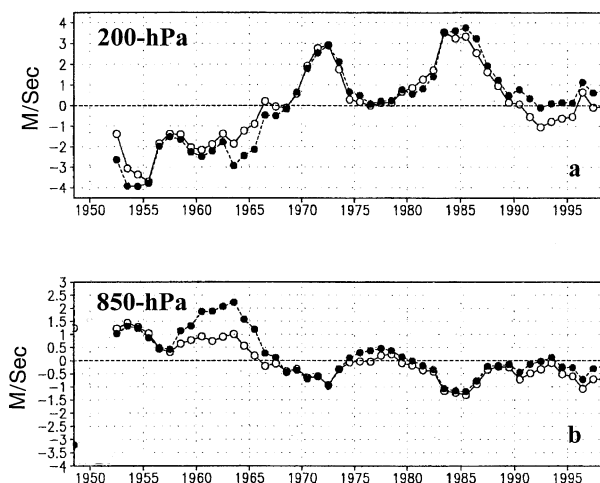

FIG. 22. JJA time series of area-averaged zonal wind anomalies over tropical northern Africa (0°–20°N, 20°W–40°E) at (a) 200 and (b) 850 hPa determined from radiosonde data (solid circles) and the NCEP–NCAR reanalysis (open circles).

cluding the Pacific Decadal Oscillation (PDO); rainfall variations over West Africa, the Amazon basin, and the tropical Pacific; surface temperature variations in the Indian Ocean, tropical Pacific, and the North Atlantic; the wintertime North Atlantic Oscillation (NAO); North American surface temperatures; Atlantic hurricane activity; and decadal variations in ENSO teleconnections.

The robustness and uniqueness of the tropical multidecadal mode has been addressed by using a variety of EOF and filtering techniques, and by comparing the results with observed station data and published results of decadal climate variability in the core regions. The temporal and spatial characteristics of this mode are found to be distinct from ENSO. The regressed global surface temperature and precipitation rate signals associated with the TMM are essentially the same whether one bases the EOF analysis on seasonal tropical 200-hPa velocity potential anomalies, or on seasonal tropical surface temperature (land + ocean) anomalies. However, if land surface temperatures anomalies are neglected in this latter calculation, the spatial correlations between the regressed SST and precipitation rate anom-

alies and those associated with the TMM drop from 0.96 to 0.7.

During JJA the positive phase of the TMM captures enhanced convection over the Amazon basin, with flanking cells of suppressed convection over West Africa and the central equatorial Pacific. During DJF enhanced convection is again observed over the Amazon basin and also over the tropical Indian Ocean, and the main area of suppressed convection is located over the central equatorial Pacific. These differences during DJF reflect the absence of the West African monsoon and the presence of enhanced convection in the area of above-average SSTs over the tropical Indian Ocean.

Because of the convective/monsoonal nature of the tropical multidecadal mode, its most direct links to the atmospheric circulation are evident in the Tropics and subtropics of both hemispheres. Characteristic convective signatures of the mode include 1) anticyclonic (cyclonic) circulation anomalies in the subtropics of both hemispheres, flanking the regions of enhanced (suppressed) tropical convection, and 2) a reversal in sign of the zonal wind anomalies between 200 and 850 hPa from the eastern Pacific to Africa.

Over the tropical and subtropical Pacific, Atlantic, and Africa, the regressed seasonal anomalies are stronger and more spatially extensive when the PC time series of the TMM and ENSO are in phase, and are weaker when the two modes are out of phase. These results suggest a substantial modulation of the ENSO teleconnections by the TMM, similar to those discussed for the North Pacific Oscillation by Gershunov and Barnett (1998). Our results indicate stronger El Niño teleconnections for the positive phase of the TMM seen during the 1980s–90s, and stronger La Niña teleconnections for the negative phase of the TMM seen during the 1950s–60s. Although the present study addresses the linear ENSO–TMM interference, the results also suggest that interactions between the two modes may help to explain the stronger El Niño episodes observed during the 1980s–90s compared to the 1950s–60s.

For the DJF season the GCM modeling study of Hoerling et al. (2001) is of particular relevance to our study. Their atmospheric simulations forced by the recent warming trend in the tropical Indian Ocean and central tropical South Pacific are consistent with the Tropics-wide SST and rainfall patterns captured by the tropical multidecadal mode. Their study also indicated that the warming trend in the tropical Indian and Pacific Oceans could be a contributing factor to the overall positive phase of the wintertime NAO seen throughout the 1980s–90s. Our results are consistent with these findings.

Our analysis additionally suggest that the TMM likely influences the NAO by modulating the upper-level confluent flow and divergent circulation within the entrance region of the North Atlantic jet steam. In particular, at high latitudes the positive phase of the TMM is associated with anomalous upper-level convergent flow across eastern Canada, which favors a more northward position of the North Atlantic jet stream and a deeper Icelandic low, both of which are consistent with the positive phase of the NAO. At lower latitudes along the southern flank of the subtropical jet stream, the positive phase of the TMM is associated with reduced upper-level westerlies and anomalous divergent outflow from enhanced tropical convection over the Amazon basin. The associated anomalous anticyclonic circulation overspreads not only the entire southern flank of the subtropical jet stream, but also extends eastward over the central North Atlantic consistent with the positive phase of the NAO. These results suggest that multidecadal fluctuations in the NAO may be forced from a combination of regions in response to the global tropical climate variability, and not necessarily one particular source region.

REFERENCES

Barnston, A. G., and R. E. Livezey, 1987: Classification, seasonality, and persistence of low frequency atmospheric circulation patterns. *Mon. Wea. Rev.,* **115,** 1083–1126.

Basist, A. N., and M. Chelliah, 1997: Comparison of tropospheric temperatures derived from the NCEP–NCAR reanalysis, NCEP operational analysis, and the Microwave Sounding Unit. *Bull. Amer. Meteor. Soc.,* **78,** 1431–1447.

Biondi, F., A. Gershunov, and D. R. Cayan, 2001: North Pacific decadal variability since 1661. *J. Climate,* **14,** 5–10.

Bjerknes, J., 1969: Atmospheric teleconnections from the equatorial Pacific. *Mon. Wea. Rev.,* **97,** 163–172.

Charney, J. G., 1975: Dynamics of deserts and drought in the Sahel. *Quart. J. Roy. Meteor. Soc.,* **101,** 193–202.

——, P. H. Stone, and W. J. Quirk, 1975: Drought in the Sahara: A biophysical feedback mechanism. *Science,* **187,** 434–435.

Chelliah, M., and P. Arkin, 1992: Large-scale interannual variability of monthly outgoing longwave radiation anomalies in the global Tropics. *J. Climate,* **5,** 372–389.

——, and C. F. Ropelewski, 2000: Reanalysis-based tropospheric temperature estimates: Uncertainties in the context of global climate change detection. *J. Climate,* **13,** 3187–3205.

Chen, T.-C, J.-H. Yoon, K. J. St. Croix, and E. S. Takle, 2001: Suppressing impacts of the Amazonian deforestation by the global circulation change. *Bull. Amer. Meteor. Soc.,* **82,** 2209–2216.

Chu, P.-S., Z.-P. Yu, and S. Hastenrath, 1994: Detecting climate change concurrent with deforestation in the Amazon basin: Which way has it gone? *Bull. Amer. Meteor. Soc.,* **75,** 579–583.

Delworth, T. L., S. Manabe, and R. J. Stouffer, 1993: Interdecadal variations in the thermohaline circulation in a coupled ocean–atmosphere model. *J. Climate,* **6,** 1993–2011.

——, ——, and ——, 1997: Multi-decadal climate variability in the Greenland Sea and surrounding regions: A coupled model simulation. *Geophys. Res. Lett.,* **24,** 257–260.

Ebisuzaki, W., M. Chelliah, and R. Kistler, 1996: NCEP/NCAR reanalysis: Caveats. *Proc. First WMO Reanalysis Workshop,* Silver Spring, MD, WMO, 81–84.

Enfield, D. B., and A. M. Mestas-Nuñez, 1999: Multiscale variabilities in global sea surface temperatures and their relationships with tropospheric climate patterns. *J. Climate,* **12,** 2719–2733.

——, ——, and R. J. Stouffer, 2001: The Atlantic multi-decadal oscillation and its relation to rainfall and river flows in the continental U.S. *Geophys. Res. Lett.,* **28,** 2077–2080.

Folland, C. K., T. N. Palmer, and D. E. Parker, 1986: Sahel rainfall and worldwide sea temperatures. *Nature,* **320,** 602–607.

Garreaud, R. D., and D. S. Battisti, 1999: Interannual (ENSO) and interdecadal (ENSO-like) variability in the Southern Hemisphere tropospheric circulation. *J. Climate,* **12,** 2113–2123.

Gershunov, A., and T. Barnett, 1998: Interdecadal modulation of ENSO teleconnections. *Bull. Amer. Meteor. Soc.,* **79,** 2715–2725.

Gill, A. E., 1982: *Atmosphere–Ocean Dynamics.* Academic Press, 662 pp.

Goldenberg, S. B., and L. J. Shapiro, 1996: Physical mechanisms for the association of El Niño and West African rainfall with Atlantic major hurricane activity. *J. Climate,* **9,** 1169–1187.

——, C. W. Landsea, A. Mestas-Nuñez, and W. M. Gray, 2001: The recent increase in Atlantic hurricane activity: Causes and implications. *Science,* **293,** 474–479.

Graham, N. E., 1994: Decadal scale climate variability in the tropical and North Pacific during the 1970s and 1980s: Observations and model results. *Climate Dyn.,* **10,** 135–162.

Gray, W. M., 1990: Strong association between West African rainfall and U.S. landfall of intense hurricanes. *Science,* **249,** 1251–1256.

——, J. D. Sheaffer, and C. W. Landsea, 1997: Climate trends associated with multi-decadal variability of Atlantic hurricane activity. *Hurricanes: Climate and Socioeconomic Impacts,* H. F. Diaz and R. W. Pulwarty, Eds., Springer-Verlag, 15–52.

Halpert, M. S., and G. D. Bell, 1997: Climate assessment for 1996. *Bull. Amer. Meteor. Soc.,* **78,** S1–S49.

Hansen, D. V., and H. F. Bezdek, 1996: On the nature of decadal anomalies in North Atlantic sea surface temperatures. *J. Geophys. Res.,* **101,** 8749–8758.

Harrison, D. E., and N. K. Larkin, 1996: The COADS sea level pressure signal: A near-global El Niño composite and time series view, 1946–1993. *J. Climate,* **9,** 3025–3055.

Hastenrath, S., 1990: Decadal-scale changes of the circulation in the tropical Atlantic sector associated with Sahel drought. *Int. J. Climatol.,* **10,** 459–472.

Higgins, R. W., A. Leetmaa, Y. Xue, and A. Barnston, 2000: Dominant factors influencing the seasonal predictability of U.S. precipitation and surface air temperature. *J. Climate,* **13,** 3994–4017.

Hoerling, M. P., J. W. Hurrell, and T. Xu, 2001: Tropical origins for recent North Atlantic climate change. *Science,* **292,** 90–92.

Hulme, M., 1995: Estimating global changes in precipitation. *Weather,* **50,** 34–42.

Hurrell, J. W., 1998: Relationships among recent atmospheric circulation changes, global warming, and satellite temperatures. *Sci. Prog.,* **81,** 205–224.

Janowiak, J. E., A. Gruber, C. R. Kondragunta, R. E. Livezey, and G. J. Huffman, 1998: A comparison of the NCEP–NCAR reanalysis precipitation and the GPCP rain gauge–satellite combined dataset with observational error considerations. *J. Climate,* **11,** 2960–2979.

Jones, P. D., T. M. L. Wigley, and G. Farmer, 1991: Marine and land temperature data sets: A comparison and look at recent trends. *Greenhouse Gas Induced Climate Change: A Critical Appraisal of Simulations and Observations,* M. E. Schlesinger, Ed., Elsevier Science, 593–602.

Kalnay, E., and Coauthors, 1996: The NCEP/NCAR 40-Year Reanalysis Project. *Bull. Amer. Meteor. Soc.,* **77,** 437–471.

Kawamura, R., 1994: A rotated EOF analysis of global sea surface temperature variability with interannual and interdecadal scales. *J. Phys. Oceanogr.,* **24,** 707–715.

——, M. Sugi, and N. Sato, 1995a: Interdecadal and interannual variability in the northern extratropical circulation simulated with the JMA global model. Part I: Wintertime leading mode. *J. Climate,* **8,** 3006–3019.

——, ——, and ——, 1995b: Interdecadal and interannual variability in the northern extratropical circulation simulated with the JMA global model. Part II: Summertime leading mode. *J. Climate,* **8,** 3006–3019.

Kistler, R., and Coauthors, 2001: The NCEP–NCAR 50-year reanalysis: Monthly means CD-ROM and documentation. *Bull. Amer. Meteor. Soc.,* **82,** 247–268.

Krishnamurti, T. N., 1971: Tropical east–west circulations during the northern summer. *J. Atmos. Sci.,* **28,** 1342–1347.

Kumar, K., B. Rajagopalan, and M. A. Cane, 1999: On the weakening relationship between the Indian Monsoon and ENSO. *Science,* **284,** 2156–2159.

Kushnir, Y., 1994: Interdecadal variations in North Atlantic sea surface temperature and associated atmospheric conditions. *J. Climate,* **7,** 141–157.

Landsea, C. W., and W. M. Gray, 1992: The strong association between western Sahel monsoon rainfall and intense Atlantic hurricanes. *J. Climate,* **5,** 435–453.

Latif, M., and T. P. Barnett, 1994: Decadal climate variability over the North Pacific and North America. *Science,* **266,** 634–637.

——, R. Kleeman, and C. Eckert, 1997: Greenhouse warming, decadal variability, or El Niño? An attempt to understand the anomalous 1990s. *J. Climate,* **10,** 2221–2239.

Lau, N.-C., and M. Nath, 1994: A modeling study of the relative roles of tropical and extratropical SST anomalies in the variability of the global atmosphere–ocean system. *J. Climate,* **7,** 1184–1207.

Livezey, R. E., and T. M. Smith, 1999: Covariability of aspects of North American climate with global sea surface temperatures on interannual to interdecadal time scales. *J. Climate,* **12,** 289–302.

Mantua, N. J., S. R. Hare, Y. Zhang, J. M. Wallace, and R. C. Francis, 1997: A Pacific interdecadal climate oscillation with impacts on salmon production. *Bull. Amer. Meteor. Soc.,* **78,** 1069–1079.

Mestas-Nuñez, A. M., and D. B. Enfield, 1999: Rotated global modes of non-ENSO sea surface temperature variability. *J. Climate,* **12,** 2734–2746.

——, and ——, 2001: Eastern equatorial Pacific SST variability: ENSO and non-ENSO components and their climate associations. *J. Climate,* **14,** 391–402.

Mo, K. C., and V. E. Kousky, 1993: Further analysis of the relationship between circulation anomaly patterns and tropical convection. *J. Geophys. Res.,* **98,** 5103–5113.

——, G. D. Bell, and W. Thiaw, 2001: Impact of sea surface temperature anomalies on the Atlantic tropical storm activity and West African rainfall. *J. Atmos. Sci.,* **58,** 3477–3496.

Morrissey, M. L., and N. E. Graham, 1996: Recent trends in rain gauge precipitation measurements from the tropical Pacific: Evidence for an enhanced hydrological cycle. *Bull. Amer. Meteor. Soc.,* **77,** 1207–1219.

Namias, J., X. Yuan, and D. R. Cayan, 1988: Persistence of North Pacific sea surface temperature and atmospheric flow patterns. *J. Climate,* **1,** 682–703.

Nicholls, N., B. Lavery, C. Fredrickson, and W. Drosdowsky, 1996: Recent apparent changes in relationships between the El Niño–Southern Oscillation and Australian rainfall and temperature. *Geophys. Res. Lett.,* **23,** 3357–3360.

Nicholson, S. E., 1996: Rainfall in the Sahel during 1994. *J. Climate,* **9,** 1673–1676.

——, and I. M. Palao, 1993: A re-evaluation of rainfall variability in the Sahel. Part I. Characteristics of rainfall variations. *Int. J. Climatol.,* **13,** 371–389.

North, G. R., T. L. Bell, R. F. Cahalan, and F. J. Moeng, 1982: Sampling errors in the estimation of empirical orthogonal functions. *Mon. Wea. Rev.,* **110,** 699–706.

Rasmusson, E. M., and T. H. Carpenter, 1982: Variations in tropical sea surface temperature and surface wind fields associated with the Southern Oscillation/El Niño. *Mon. Wea. Rev.,* **110,** 354–384.

Ropelewski, C. F., M. S. Halpert, and X. Wang, 1992: Observed tropospheric biennial variability and its relationship to the Southern Oscillation. *J. Climate,* **5,** 594–614.

Rowell, D. P., C. K. Folland, K. Maskell, and N. M. Ward, 1995: Variability of summer rainfall over tropical North Africa 1906–92: Observations and modeling. *Quart. J. Roy. Meteor. Soc.,* **121,** 669–704.

Shinoda, M., 1990: Long-term variability of the tropical African rain belt and its relation to rainfall in the Sahel and northern Kalahari. *J. Meteor. Soc. Japan,* **68,** 19–35.

——, 1995: West African rain belt variations: An update to 1990. *J. Meteor. Soc. Japan,* **73,** 259–266.

Smith, T. M., R. W. Reynolds, R. E. Livezey, and D. C. Stokes, 1996: Reconstruction of historical sea surface temperatures using empirical orthogonal functions. *J. Climate,* **9,** 1403–1420.

Thaiw, W. M., J. V. Kousky, and V. Kumar, 1998: Atmospheric circulation associated with recent Sahelian hydrologic anomalies. *Proc. Abidjan'98 Conf. on Water Resources Variability in Africa in the XXth Century,* Abidian, Ivory Coast, IAHS Publication 252, 63–67.

Trenberth, K. E., 1990: Recent observed interdecadal climate changes in the Northern Hemisphere. *Bull. Amer. Meteor. Soc.,* **71,** 988–993.

——, and J. W. Hurrell, 1994: Decadal atmosphere–ocean variations in the Pacific. *Climate Dyn.,* **9,** 303–319.

van Loon, H., and D. J. Shea, 1985: The Southern Oscillation. Part IV: The precursors south of 15°S to the extremes of the oscillation. *Mon. Wea. Rev.,* **113,** 2063–2074.

Ward, M. N., 1998: Diagnosis and short-lead time prediction of summertime rainfall in tropical North Africa at interannual and multidecadal time scales. *J. Climate,* **11,** 3167–3191.

Wright, P. B., J. M. Wallace, T. P. Mitchell, and C. Deser, 1988: Correlation structure of the El Niño/Southern Oscillation phenomenon. *J. Climate,* **1,** 609–626.

Xie, P., and P. A. Arkin, 1997: Global precipitation: A 17-year monthly analysis based on gauge observations, satellite estimates, and numerical model outputs. *Bull. Amer. Meteor. Soc.,* **78,** 2539–2558.

Xue, Y., and J. Shukla, 1993: The influence of land surface properties on Sahel climate. Part I: Desertification. *J. Climate,* **6,** 2232–2245.

Zeng, N., and J. D. Neelin, 2000: The role of vegetation–climate interaction and interannual variability in the shaping of the African savanna. *J. Climate,* **13,** 2665–2670.

——, ——, K.-M. Lau, and C. J. Tucker, 1999: Enhancement of interdecadal climate variability in the Sahel by vegetation interaction. *Science,* **286,** 1537–1540.

Zhang, Y., J. M. Wallace, and D. S. Battisti, 1997: ENSO-like interdecadal variability: 1900–93. *J. Climate,* **10,** 1004–1020.